

THE REFRACTIVE INDEX OF  $Pb_{1-x}Sn_xTe$ ,  
 $Pb_{1-y}Sn_ySe$ , AND  $PbS_{1-x}Se_x$  AND  
THEORETICAL CALCULATIONS FOR  $Pb_{1-x}Sn_xTe$   
AND  $Pb_{1-y}Sn_ySe$  10.6 MICRON HETEROSTRUCTURE  
INJECTION LASERS

Walter George Opyd

POSTGRADUATE SCHOOL  
Y, CALIF. 93940

# NAVAL POSTGRADUATE SCHOOL

## Monterey, California



# THESIS

The Refractive Index of  $Pb_{1-x}Sn_xTe$ ,  
 $Pb_{1-y}Sn_ySe$ , and  $PbS_{1-x}Se_x$  and  
Theoretical Calculations for  $Pb_{1-x}Sn_xTe$   
and  $Pb_{1-y}Sn_ySe$  10.6 Micron Heterostructure  
Injection Lasers

by

Walter George Opyd

Thesis Advisor:

Tien Fan Tao

June 1973

Approved for public release; distribution unlimited.

T155223



The Refractive Index of  $Pb_{1-x}Sn_xTe$ ,  $Pb_{1-y}Sn_ySe$ , and  
 $PbS_{1-x}Se_x$  and Theoretical Calculations for  
 $Pb_{1-x}Sn_xTe$  and  $Pb_{1-y}Sn_ySe$  10.6 Micron Heterostructure  
Injection Lasers

by

Walter George Opyd  
Ensign, United States Navy  
B.S.E.E., United States Naval Academy, 1972

Submitted in partial fulfillment of the  
requirements for the degree of

MASTER OF SCIENCE IN ELECTRICAL ENGINEERING

from the

NAVAL POSTGRADUATE SCHOOL

June 1973

Thes.s  
9583  
G-1

ABSTRACT

In the first part of this work, the refractive indices,  $n$ , in the fundamental absorption edge regions of three alloy semiconductors,  $\text{Pb}_{1-x}\text{Sn}_x\text{Te}$ ,  $\text{Pb}_{1-y}\text{Sn}_y\text{Se}$ , and  $\text{PbS}_{1-x}\text{Se}_x$ , were investigated. Preliminary results of the refractive indices of  $\text{PbS}_{1-x}\text{Se}_x$  thin films are presented. For  $\text{Pb}_{1-x}\text{Sn}_x\text{Te}$  and  $\text{Pb}_{1-y}\text{Sn}_y\text{Se}$ , empirical relationships for  $n$  have been determined as a function of wavelength, composition, and temperature, using refractive index data previously measured in this laboratory.

In the second part of this work, the laser performances of double heterojunction  $\text{Pb}_{1-x}\text{Sn}_x\text{Te}$  and  $\text{Pb}_{1-y}\text{Sn}_y\text{Se}$  injection lasers emitting  $10.6\mu$  radiation and operated at  $85^{\circ}\text{K}$ , were theoretically calculated. Threshold current and lasing output power as functions of compositions and laser geometry, were calculated as a guide for optimum design. Threshold current densities of less than  $200\text{A}/\text{cm}^2$  and output power of more than  $2\text{mW}$  with  $1\text{A}$  bias current were calculated for diodes of  $1\text{mm}^2$  cross section, operated at  $85^{\circ}\text{K}$ .



TABLE OF CONTENTS

I.	OPTICAL PROPERTIES -----	9
	A. INTRODUCTION -----	9
	B. THEORY -----	10
	1. Electromagnetic Theory of Optical Properties -----	10
	2. Principles of Experimental Technique --	14
	C. EMPIRICAL REFRACTIVE INDEX RELATIONSHIPS FOR $Pb_{1-x}Sn_xTe$ and $Pb_{1-y}Sn_ySe$ -----	15
	1. $Pb_{1-x}Sn_xTe$ -----	15
	2. $Pb_{1-y}Sn_ySe$ -----	17
	D. MEASUREMENTS OF $PbS_{1-x}Se_x$ -----	19
	1. Thin Film Preparation -----	19
	2. Transmission Measurements -----	21
	3. Thickness Determination -----	21
	4. Discussion of Results -----	22
II.	HETEROJUNCTION LASERS -----	24
	A. INTRODUCTION -----	24
	B. HETEROJUNCITON -----	25
	1. Structure -----	25
	2. Band Diagram -----	26
	3. Junction Capacitance and Current-Voltage Characteristics -----	27
	4. Electro-Optic Interest in Heterojunctions	29
	C. THEORY OF SEMICONDUCTOR INJECTION LASERS --	31
	1. Principles of Operation -----	31
	2. Three Layer Dielectric Waveguide Model	34
	3. Design Equations -----	40



D. THRESHOLD AND POWER CALCUALTIONS -----	41
1. Estimation of Laser Parameters -----	42
a. Linewidth -----	42
b. Refractive Index -----	42
c. Free Carrier Absorption -----	43
d. Internal Quantum Efficiency -----	44
e. Demerit Factor -----	44
f. Active Region Thickness -----	45
g. Homojunction Refractive Index Discontinuity -----	45
2. Threshold Current -----	46
3. External Quantum Efficiency -----	47
4. Output Power -----	48
E. OBSERVATIONS -----	50
1. Design Tradeoffs -----	50
a. Composition -----	50
b. Carrier Concentration -----	51
c. Active Region Thickness -----	52
d. Cavity Length -----	53
e. Cavity Width -----	53
2. State of Narrow-Gap Laser Operation --	54
DRAWINGS -----	56
LIST OF REFERENCES -----	87
INITIAL DISTRIBUTION LIST -----	90
FORM DD 1473 -----	91



## LIST OF TABLES

### TABLE

1.	Pb <sub>1-x</sub> Se <sub>x</sub> Optical Samples -----	20
2.	Theoretical DH Laser Calculations -----	49
3.	State of Pb <sub>1-x</sub> Sn <sub>x</sub> Te Injection Lasers -----	55



## LIST OF DRAWINGS

### FIGURE

1-1	Index of Refraction of PbTe -----	56
1-2	Index of Refraction of Pb <sub>.94</sub> Sn <sub>.06</sub> Te -----	57
1-3	Index of Refraction of Pb <sub>.88</sub> Sn <sub>.12</sub> Te -----	58
1-4	Index of Refraction of Pb <sub>.76</sub> Sn <sub>.24</sub> Te -----	59
1-5	Peak Refractive Index as a Function of Temperature for Pb <sub>1-x</sub> Sn <sub>x</sub> Te -----	60
1-6	Peak Refractive Index as a Function of Composition for Pb <sub>1-x</sub> Sn <sub>x</sub> Te -----	60
1-7	Peak Photon Energy as a Function of Temperature for Pb <sub>1-x</sub> Sn <sub>x</sub> Te -----	61
1-8	Peak Photon Energy as a Function of Composition for Pb <sub>1-x</sub> Sn <sub>x</sub> Te -----	61
1-9	Index of Refraction of PbSe -----	62
1-10	Index of Refraction of Pb <sub>.965</sub> Sn <sub>.035</sub> Se -----	63
1-11	Index of Refraction of Pb <sub>.935</sub> Sn <sub>.065</sub> Se -----	64
1-12	Index of Refraction of Pb <sub>.9</sub> Sn <sub>.1</sub> Se -----	65
1-13	Index of Refraction of PbS <sub>.8</sub> Se <sub>.2</sub> -----	66
1-14	Index of Refraction of PbS <sub>.64</sub> Se <sub>.36</sub> -----	67
1-15	Index of Refraction of PbS <sub>.4</sub> Se <sub>.6</sub> -----	68
2-1	Heterojunction Band Diagram -----	69
2-2	Three Layer Dielectric Waveguide Model -----	70
2-3	Normalized Transverse Propagation Constant For Region 2 -----	71
2-4	Normalized Transverse Propagation Constant For Region 1 -----	72
2-5	Normalized Transverse Propagation Constant For Region 3 -----	73



2-6	Loss Factor for Region 1 -----	74
2-7	Loss Factor for Region 3 -----	75
2-8	Refractive Index and Absorption coefficient of $Pb_{1-y}Sn_ySe$ at $10.6\mu$ -----	76
2-9	Refractive Index and Absorption Coefficient of of $Pb_{1-x}Sn_xTe$ at $10.6\mu$ -----	77
2-10	Threshold Current Density as a Function of Active Region Thickness for DH $Pb_{1-x}Sn_xTe$ Lasers	78
2-11	Threshold Current Density as a Function of Active Region Thickness for DH $Pb_{1-y}Sn_ySe$ Lasers	79
2-12	Threshold Current Density for $Pb_{1-x}Sn_xTe$ DH Lasers of Various Lengths. -----	80
2-13	External Quantum Efficiency as a Function of Active Region Thickness for $Pb_{1-y}Sn_ySe$ DH Lasers	81
2-14	External Quantum Efficiency as a Function of Active Region Thickness for $Pb_{1-x}Sn_xTe$ DH Lasers	82
2-15	Threshold Current and External Quantum Efficiency as Functions of Cavity Length for DH $Pb_{1-x}Sn_xTe$ Lasers, $x_{1.3} = 0$ , $n_{1.3} = 5 \times 10^7$ cm <sup>-3</sup> -----	83
2-16	Output Power as a Function of Bias Current For $Pb_{1-x}Sn_xTe$ and $Pb_{1-y}Sn_ySe$ Injection Lasers (Log-Log Plot) -----	84
2-17	Output Power as a Function of Bias Current for $Pb_{1-x}Sn_xTe$ Injection Lasers (Linear Plot) -----	85
2-18	Output Power as a Function of Bias Current for $Pb_{1-y}Sn_ySe$ Injection Lasers (Linear Plot) -----	86



#### ACKNOWLEDGEMENTS

Professor T. F. Tao deserves much credit for his direction of the work upon which this thesis is based. The optical samples analyzed were prepared by Raymond Zahm. Much thanks is also due Professor John Schultz and Robert Sanders of the Department of Material Science and Chemistry for their valuable assistance concerning the operation of the Perkin-Elmer Spectrophotometer. This research was made possible by the support of the Office of Naval Research.

Finally, I would like to express my appreciation to my wife, Nancy, for long hours of typing and proof reading this work.



## I. OPTICAL PROPERTIES

### A. INTRODUCTION

In the last few years much interest has been generated in the IV-VI semiconducting alloys  $Pb_{1-x}Sn_xTe$ ,  $Pb_{1-y}Sn_ySe$ , and  $PbS_{1-x}Se_x$ . By controlling the composition of these semiconductors, the energy gap can be varied. For  $Pb_{1-x}Sn_xTe$  and  $Pb_{1-y}Sn_ySe$ , it can be adjusted to any value between 0.3 eV and 0 eV. Laser emission has been achieved over the infrared spectral range of 3.9 to 31.8 microns using these alloys [1,2]. This wide range of tuneability has invited many uses.

Groups at M.I.T.'s Lincoln Laboratory have used  $PbS_{1-x}Se_x$  diode lasers for high-resolution spectroscopy of nitric oxide [3], carbon monoxide [4], and water vapor and use is suggested for carbon dioxide and ozone[5]. Since listed above are four major pollutants,  $PbS_{1-x}Se_x$  would seem an obvious material to be considered for use in a pollution monitoring system.

The combination of the 8 to 14 micron atmospheric window and the high power and high stability  $CO_2$  laser source at 10.6 microns makes an infrared laser radar or communication system operating at 10.6 microns attractive. For detection in this spectral range, fast and sensitive  $Pb_{1-x}Sn_xTe$  and  $Pb_{1-y}Sn_ySe$  photovoltaic detectors have been fabricated[6]. With heterodyne methods, detection approaching



photon counting has been achieved [7].  $\text{Pb}_{1-x}\text{Sn}_x\text{Te}$  diode lasers have been successfully heterodyned with both  $\text{CO}_2$  lasers and other  $\text{Pb}_{1-x}\text{Sn}_x\text{Te}$  diode lasers [2].

An important parameter in calculating the maximum efficiency of a photodetector is the refractive index of the material used. This parameter is necessary in diode laser calculations of the modes amplified, the threshold current required, the optical confinement of the stimulated radiation, and the pattern of radiation from the emitting facets. It is also useful in the optimal design of an efficient laser diode. Because of their narrow energy gaps, efficient operations of  $\text{Pb}_{1-x}\text{Sn}_x\text{Te}$ ,  $\text{Pb}_{1-y}\text{Sn}_y\text{Se}$ , and  $\text{PbS}_{1-x}\text{Se}_x$  devices have not been achieved above liquid nitrogen temperatures. For this reason, knowledge of the refractive index as a function of temperature would be beneficial. This can be used in refined design and improvement of these lasers.

One objective of this work is to provide empirical refractive index information for  $\text{Pb}_{1-x}\text{Sn}_x\text{Te}$ ,  $\text{Pb}_{1-y}\text{Sn}_y\text{Se}$ , and  $\text{PbS}_{1-x}\text{Se}_x$  as a function of composition, wavelength, and temperature in their fundamental absorption edge regions.

## B. THEORY

### 1. Electromagnetic Theory of Optical Properties

The parameters referred to as the optical properties of a material are based on the propagation of electromagnetic waves through the material in question. The theory of propagation of electromagnetic radiation in a material can be described by Maxwell's field equations,



$$\nabla \times \bar{E} = -\mu \frac{\partial \bar{H}}{\partial t}, \quad (1-1a)$$

$$\nabla \times \bar{H} = (\epsilon - j\frac{\sigma}{\omega}) \frac{\partial \bar{E}}{\partial t}, \quad (1-1b)$$

$$\nabla \cdot \bar{E} = \frac{\rho}{\epsilon}, \quad (1-1c)$$

$$\nabla \cdot \bar{H} = 0. \quad (1-1d)$$

where  $\bar{E}$  and  $\bar{H}$  are the electric and magnetic field vectors,  $\epsilon = \epsilon_r \epsilon_0$  and  $\mu = \mu_r \mu_0$  are the permittivity and permeability, and  $\sigma$  is the conductivity using the rationalized MKS system of units. Vectors are indicated by a bar and complex quantities by a tilde symbol. The divergence of  $\bar{E}$  can be considered equal to zero for the case under consideration since there can be no permanent charge density in a conductor. For the nonmagnetic materials considered here  $\mu_r = 1$ . Moss gives a thorough treatment of this case [8].

From equations (1-1) the wave equation can be derived,

$$\nabla^2 \bar{E} = \mu (\epsilon - j\frac{\sigma}{\omega}) \frac{\partial^2 \bar{E}}{\partial t^2}. \quad (1-2)$$

A similar equation can be obtained for  $\bar{H}$ .

A solution for a wave propagation in the positive  $\bar{s}$  direction is

$$\bar{E} = \bar{E}_0 e^{j\omega(t - \frac{1}{v}(\bar{r} \cdot \bar{s}))}, \quad (1-3)$$

where  $\omega$  is the radian frequency of the radiation,  $v$  is the propagation velocity,  $\bar{r}$  is the position vector, and  $\bar{s}$  is a unit vector in the direction of propagation.

This solution requires that

$$\frac{1}{v^2} = \mu (\epsilon - j\frac{\sigma}{\omega}). \quad (1-4)$$



The index of refraction of the material is given by  $\tilde{n} = c/v$ , where  $c$  is the free space velocity of light. Hence,

$$\tilde{n}^2 = (\epsilon_r - j \frac{\sigma}{\omega \epsilon_0}) . \quad (1-5)$$

This is often referred to as the complex dielectric constant,

$$\tilde{\epsilon} = \epsilon' - j \epsilon'' , \quad (1-6a)$$

where  $\epsilon' = \epsilon_r$  ,  $\epsilon'' = \frac{\sigma}{\omega \epsilon_0}$  .  $\quad (1-6b)$

and  $\epsilon'' = \frac{\sigma}{\omega \epsilon_0}$  .  $\quad (1-6c)$

In general, the refractive index will be complex and can be expressed as

$$\tilde{n} = n - j \kappa . \quad (1-7)$$

In the following discussions the term "refractive index" without the adjective "complex" preceding it will refer to the real part of the complex index of refraction. The imaginary part of the complex refractive index is called the extinction coefficient.

It can be seen that the propagation of an electromagnetic wave in a medium can be described either in terms of  $n$  and  $\kappa$ , known as the optical constants of the medium, or in terms of  $\epsilon'$  and  $\epsilon''$ , referred to as the electromagnetic constants of the medium. The relationships between these constants are:

$$\epsilon' = n^2 - \kappa^2 , \quad (1-8a)$$

$$\epsilon'' = 2n\kappa , \quad (1-8b)$$

$$n = \left[ \frac{1}{2} \left( (\epsilon'^2 + \epsilon''^2)^{\frac{1}{2}} + \epsilon' \right) \right]^{\frac{1}{2}} , \quad (1-8c)$$



$$\kappa = \left[ \frac{1}{2} ((\epsilon'^2 + \epsilon''^2)^{\frac{1}{2}} - \epsilon') \right]^{\frac{1}{2}}. \quad (1-8d)$$

By replacing  $\nu$  with  $c/\tilde{n}$  in equation (1-3)  $\bar{E}$  is found to contain an attenuation factor of  $e^{-\omega\kappa(\tilde{r} \cdot \tilde{s})/c}$ . The absorption coefficient,  $\alpha$ , is defined such that the energy in an electromagnetic wave decreases by a factor of  $e^{-\alpha}$  in a distance of  $1/\alpha$ . The energy contains two attenuation factors, one for  $\bar{E}$  and one for  $\bar{H}$ , therefore,

$$\alpha = 2\omega\kappa/c = 4\pi\kappa/\lambda, \quad (1-9)$$

where  $\lambda$  is the free space wavelength of the radiation.

The real and imaginary parts of the complex index of refraction are not independent. They are related by the Kramers-Kronig relations, also known as the dispersion relations [8],

$$n(E_0) = 1 + \frac{2}{\pi} \int_0^\infty \frac{\kappa(E)E}{E^2 - E_0^2} dE, \quad (1-10a)$$

$$\kappa(E_0) = \frac{2}{\pi} \int_0^\infty \frac{n(E)E_0}{E_0^2 - E^2} dE. \quad (1-10b)$$

Hence, the behavior of the refractive index can be deduced from the behavior of the extinction coefficient. Equation (1-10a) can be rewritten [9],

$$n(E_0) = 1 + \frac{\lambda c}{2\pi E_0} \int_0^\infty \left[ \left( \frac{d\alpha(E)}{dE} \right) \times \ln \left( \frac{E+E_0}{TE-E_0} \right) \right] dE. \quad (1-11)$$

In this form it can be seen that in the spectral range of a sharp absorption edge there will also be a change in refractive index. This accounts for the dispersion of



the index of refraction in the fundamental absorption edge region of the semiconductors investigated.

## 2. Principles of Experimental Techniques

The refractive index of  $\text{PbS}_{1-x}\text{Se}_x$  was obtained by measuring the transmittance through thin films [10]. Interference fringes are observed in the transmittance spectrum for thin films several microns thick. This interference is the result of multiple internal reflections of the radiation within the film before being transmitted or absorbed. For a condition of maximum constructive interference, the light transmitted on its first pass across the film must be in phase with light that requires additional round trips across the film and back before being transmitted. This is equivalent to

$$2d\beta = 2\pi m, \quad (1-12)$$

where  $\beta = 2\pi n/\lambda$  is the phase constant within the film,  $d$  is the film thickness, and  $m$  is an integer. Substituting for  $\beta$ , one obtains

$$2nd = m\lambda. \quad (1-13)$$

The integer  $m$  is known as the fringe order and must be known along with  $d$  and  $\lambda$  in order to determine  $n$ . The fringe order can be determined by observing the wavelengths of two successive low order fringes. From equation (1-13)

$$\frac{m\lambda_m}{(m+1)\lambda_{m+1}} = \frac{n_m}{n_{m+1}}, \quad (1-14a)$$



or

$$m = \lambda_{m+1} / \left( \left( \frac{n_{m+1}}{n_m} \right) \lambda_m - \lambda_{m+1} \right) . \quad (1-14b)$$

For two successive low-order fringes the change in  $n$  is usually small and  $n_{m+1}/n_m$  can be approximated by a number a few percent larger than unity without introducing ambiguity in  $m$ .

### C. EMPIRICAL REFRACTIVE INDEX RELATIONSHIPS FOR

$Pb_{1-x}Sn_xTe$  AND  $Pb_{1-y}Sn_ySe$

#### 1. $Pb_{1-x}Sn_xTe$

Refractive indices of  $Pb_{1-x}Sn_xTe$  for five compositions,  $x=0, 0.06, 0.12, 0.18$ , and  $0.24$ , have been determined by Walz of this laboratory [13] at three temperatures,  $80^{\circ}K$ ,  $195^{\circ}K$ , and  $300^{\circ}K$ . The measured values of  $n$  are presented as a function of wavelength,  $\lambda$ , in figures (1-1) through (1-4) for  $x=0, 0.06, 0.12$ , and  $0.24$ , respectively. It should be noted that  $x=0.18$  data is not presented because it was found to be inconsistent with data of other compositions. The composition of the samples for which  $x$  was assumed to be  $0.18$  may have been in error.

In this thesis, attempts were made to search for empirical relationships expressing  $n$  as functions of  $\lambda$ ,  $x$ , and  $T$ . It was found that for  $Pb_{1-x}Sn_xTe$  samples of typical carrier concentrations in the high  $10^{17}$  to low  $10^{18} \text{ cm}^{-3}$  range, refractive indices near the fundamental absorption



edge can be approximated by the following three relationships, equations (1-15), (1-16), and (1-17).

The variation of  $n$  with  $\lambda$  is given in terms of  $n_p$  and  $E_p$  by

$$n = 0.0133(1.24/E_p - \lambda) + 0.675/(|1.24/E_p - \lambda| + 1.5) - .45 + n_p \quad (1-15)$$

where  $n_p$  is the peak refractive index which depends upon  $x$  and  $T$  as

$$n_p = 6.49 - 1.59 \times 10^{-3}T + 2.78x \quad (1-16)$$

and  $E_p$  is the photon energy at which the refractive index peak occurs, which depends upon  $x$  and  $T$  as

$$E_p = 0.19 + 4.52 \times 10^{-4}T - 0.568x + 5.8x^4. \quad (1-17)$$

These three relationships are obtained from the measured results presented in figures (1-1) to (1-4) in the following manner. Plotting  $n_p$  vs.  $T$  and  $n_p$  vs.  $x$ , as shown in figures (1-5) and (1-6), respectively, indicated linear dependencies of  $n_p$  on both of these parameters. Also, a linear dependency of  $E_p$  upon  $T$  was observed as shown in figure (1-7). The variation of  $E_p$  with  $x$  was found to deviate somewhat from linear dependence for larger percentages of SnTe as shown in figure (1-8). The  $x^4$  term in equation (1-17) is an attempt to account for this.

Equation (1-17) for  $E_p$  differs only by a constant from an equation for the optical energy gap,  $E_g$ , as determined by Tao [14]. A review of all the data that have been reported on the optical energy gap of  $Pb_{1-x}Sn_xTe$  lead Tao



to the following empirical relation:

$$E_g = 0.181 + 4.52 \times 10^{-4} T - 0.568x + 5.8x^4. \quad (1-18)$$

The  $x^4$  term is believed to be due to the Burnstein shifts since it has not been observed in laser emission.

The calculated refractive indices using the empirical relationships are presented as solid curves in figures (1-1) through (1-4) in which the measured refractive index data are also presented as comparisons.

## 2. Pb<sub>1-y</sub>Sn<sub>y</sub>Se

Refractive indices of Pb<sub>1-y</sub>Sn<sub>y</sub>Se for four compositions,  $y=0$ ,  $.035$ ,  $.065$ , and  $0.1$ , have been determined by Kim [12] at five temperatures,  $80^{\circ}\text{K}$ ,  $150^{\circ}\text{K}$ ,  $200^{\circ}\text{K}$ ,  $250^{\circ}\text{K}$ , and  $300^{\circ}\text{K}$ . The measured values of  $n$  are presented as a function of wavelength,  $\lambda$ , in figures (1-9) through (1-12) for  $y=0$ ,  $0.035$ ,  $0.065$ , and  $0.1$  respectively.

Attempts to find empirical relationships expressing  $n$  in terms of  $\lambda$ ,  $y$ , and  $T$  resulted in the following three relationships for samples of carrier concentrations on the order of high  $10^{17} \text{ cm}^{-3}$  to low  $10^{18} \text{ cm}^{-3}$ .

$$n = 0.0133 (1.24/E_p - \lambda) + 1.5/(|1.24/E_p - \lambda| + 3.0) - 0.5 + n_p, \quad (1-19)$$

$$n_p = 5.49 - 1.49 \times 10^{-3} T + 3.76y, \quad (1-20)$$

$$E_p = 0.145 + 4.65 \times 10^{-4} T - 0.85y. \quad (1-21)$$

These results were determined in the same manner as those for Pb<sub>1-x</sub>Sn<sub>x</sub>Te in section I-C-1. These empirical



relationships were used to determine the solid curves presented on the plots of measured refractive index data in figures (1-9) through (1-12).

As in the case of  $Pb_{1-x}Sn_xTe$ ,  $E_p$  differs only by a constant from the expression for  $E_g$  of  $Pb_{1-y}Sn_ySe$  as determined by Tao [14]. Tao has represented the optical energy gap by

$$E_g = 0.135 + 4.65 \times 10^{-4} - 0.85y. \quad (1-22)$$



## D. MEASUREMENTS ON $\text{PbS}_{1-x}\text{Se}_x$

### 1. Thin Film Preparation

The pseudobinary system of  $\text{PbS}_{1-x}\text{Se}_x$  forms a complete series of solid solutions in the rocksalt structure [11]. Three compositions of the semiconductor were studied. They included  $x = 0.2, 0.36$  and  $0.6$ . Films ranging in thickness from 1 to 7 microns were deposited on freshly cleaved substrates of  $\text{NaCl}$  and  $\text{KCl}$ . The substrates were approximately one square centimeter in area and two millimeters thick. Film preparation was by a one-boat evaporation method.

Back-reflection Laue patterns revealed that all of the samples are single crystals by the absence of Debye ring. The composition of the samples was investigated by the x-ray diffractometer recordings.

All samples were prepared from stoichiometric source material yielding n-type conductivity. Carrier concentrations determined by Hall measurements were on the order of  $10^{18} \text{ cm}^{-3}$ . Table 1 lists the composition, thickness, and substrate for the samples tested.

In general, the films appeared shiny and flat. Some had minute cleavage steps and pinholes but it is not believed that these defects would alter the positioning of the interference fringes. A few of the samples used had a slight hazy appearance and some not used were covered with a black film. It is believed that this was finely divided lead precipitated on the film surface due to the substrate being at a temperature below the solubility limit for the



TABLE 1

 $PbS_{1-x}Se_x$  OPTICAL SAMPLES

SAMPLE NUMBER	X	SUBSTRATE	THICKNESS ( $\mu$ )
1	0.2	KCl	1.23
2	0.36	NaCl	6.85
3	0.6	KCl	1.66



lead content of the source material. This precipitation of lead would be consistent with the retrograde solubility determined for lead in PbS and PbSe [11].

## 2. Transmission Measurements

Optical measurements were made in the  $2.5$  to  $20\mu$  region of the infrared spectrum using a Perkin-Elmer 621 grating infrared spectrophotometer. Films were held in the sample beam by a pressure contact to the cold-finger of a liquid nitrogen dewar.

Transmittance measurements were made at four temperatures,  $80^\circ\text{K}$ ,  $150^\circ\text{K}$ ,  $230^\circ\text{K}$ , and  $300^\circ\text{K}$ , for  $x=.2$  and at three temperatures,  $80^\circ\text{K}$ ,  $180^\circ\text{K}$ , and  $300^\circ\text{K}$ , for  $x=.36$  and  $x=.6$ . Temperature was monitored by a copper-constantan thermocouple mounted on the cold-finger along side the film. Temperatures were maintained to within  $\pm 2^\circ\text{K}$ . The dewar used is described elsewhere [12,13]. Frequency resolution of a scan was limited by the speed of the amplifier in response to a change in transmittance. Scan time was set to 32 minutes for the entire  $2.5$  to  $50\mu$  range of the spectrophotometer. The scan was terminated manually at  $20\mu$ , however, due to the cutoff of the substrate. Frequency resolution was estimated to be better than  $5\text{cm}^{-1}$  at  $2000\text{cm}^{-1}$ .

## 3. Thickness Determination

In using the interference fringe method to determine the refractive index, equation ( 1 - 13 ) shows a linear dependence upon the reciprocal of the film thickness. Due to the certainty of fringe order and high accuracy in



wavelength the percentage of error in the index of refraction is approximately equal to the percentage of error in thickness. Once the refractive index of a material is known the thickness can be determined reliably thereafter by using the interference fringe method and solving equation (1-13) for d.

To provide reliable thickness measurements for this work, a scanning electron microscope was used. After transmission measurements, each sample was cleaved across the region where the optical measurements had been made. The film-substrate cross-section was then coated with a thin layer of gold. With the electron beam focused on the cross-section, the semiconductor film was observed as a bright region corresponding to high reflection of the beam. The layer of gold was used to prevent the accumulation of electrons in the dielectric substrate which would have resulted in very bright reflective regions and made the scanning electron microscope picture not useful for the determination of film thickness.

#### 4. Discussion of Results

Refractive index data for the three compositions of  $\text{PbS}_{1-x}\text{Se}_x$  studied is presented in figures (1-13) through (1-15). The compositions indicated are those of the source materials. Uncertainty in the absolute magnitudes is estimated to be less than  $\pm 5\%$ . This is primarily a result of uncertainty in film thickness due to ambiguities in scanning electron microscope photographs. The relative



error of the positioning of data is probably less than  $\pm$  1% due to the certainty of position for interference fringe extrema.

A peak in the refractive index was observed at an energy near the optical energy gap. The shift of the peak energy displayed a positive temperature coefficient and negative composition coefficient. The absolute magnitude of the refractive index, on the other hand, displayed a negative temperature coefficient and positive composition coefficient.



## II. HETEROJUNCTION LASERS

### A. INTRODUCTION

Maximum channel capacity in the electromagnetic transmission of information is limited by carrier frequency. The range resolution of a radar system is also limited by carrier frequency. The security of a communication system and the azimuth resolution of a radar system or illuminator are limited by beamwidth. These considerations make operation at optical frequencies, by the use of lasers, very attractive for line-of-sight systems. Although the atmospheric absorption severely attenuates light in much of the optical spectrum, the high power and high stability CO<sub>2</sub> laser operates at a wavelength of 10.6 microns which is well within the 8 to 14 micron atmospheric window.

Using coherent detection, the theoretical quantum limit of minimum detectable power, i.e., photon counting, can be approached by providing sufficient local oscillator power. Minimum detectable power within a factor of five of the theoretical quantum limit has been experimentally observed with a local oscillator power of 1.5 milliwatts [7].

The Pb<sub>1-x</sub>Sn<sub>x</sub>Te diode laser has been fine tuned about 10.6 microns and optically heterodyned with a CO<sub>2</sub> laser [2]. Optical power in excess of 1.5 milliwatts has also been reported for Pb<sub>1-x</sub>Sn<sub>x</sub>Te laser diodes [2]. However, threshold current densities of less than 1000A/cm<sup>2</sup> and CW



operation has not been reported for  $Pb_{1-x}Sn_xTe$  laser diodes operated at liquid nitrogen temperatures. This may be made possible by the use of heterostructure which also has not been reported for laser diodes in this spectral range. The objective of this part of the thesis research is to make theoretical calculations of the performance of 10.6 micron  $Pb_{1-x}Sn_xTe$  and  $Pb_{1-y}Sn_ySe$  heterojunction injection lasers operated at liquid nitrogen temperatures in order to estimate their feasibilities and suggest criteria for optimal design.

#### B. HETEROJUNCTIONS

The following general discussion of heterojunction basics is extracted primarily from a comprehensive review article by T.L. Tansley [15]. A heterojunction, given its name by R.L. Anderson of IBM in 1960, is any junction formed between two semiconductors excluding the case of both materials being identical or differing only in conductivity type.

##### 1. Structure

Some of the methods of fabrication used for homojunction are also used for heterojunctions, i.e., the interface alloy technique, solution-growth technique, vapor-phase epitaxy, liquid-phase epitaxy, and vacuum deposition. Liquid-phase epitaxy is the primary method used for high quality heterojunction diode lasers [2, 16].

A perfect match in lattice constants and thermal expansion coefficients is not normally possible to attain when two materials are chosen for a heterojunction. The



result is interface states at the junction. Interface states may cause the practical operation of a device to deviate considerably from that expected for a theoretical model.

Heterojunctions may be formed by two materials of the same conductivity type. These are known as isotype heterojunctions. The junctions considered in examples to follow are between materials of opposite conductivity type in which case the structures are known as anisotype heterojunctions.

## 2. Band Diagram

The energy band diagram at equilibrium, i.e., no applied voltage, is determined by the conditions that the Fermi level must be constant and that the vacuum level must be continuous and parallel to the band edges. Figure (2-1a) shows two isolated semiconductors, one p-type and one n-type. In figure (2-1b) they are joined to form an ideal p-n junction where:

$E_F$  = Fermi level,

$E_{ci}$  = conduction band in semiconductor i,

$E_{vi}$  = valence band in semiconductor i,

$qV_{bi}$  = built-in potential supported in semiconductor i,

$\chi_i$  = electron affinity of semiconductor i,

$\Delta E_c$  = conduction band discontinuity,

$\Delta E_v$  = valence band discontinuity.

It can be seen that the band discontinuities are given by



$$\Delta E_c = \chi_2 - \chi_1, \quad (2-1a)$$

$$\Delta E_v = (E_g 2 + \chi_2) - (E_g 1 + \chi_1), \quad (2-1b)$$

where  $E_g = E_c - E_v$

### 3. Junction Capacitance and Current-Voltage Characteristics

As in the homojunction, a depletion region is established on both sides of the junction as a result of the equilibrium between drift and diffusion currents. The associated electric field is normal to the junction requiring a boundary condition of continuity of the electrical displacement vector across the junction, i.e.,  $\epsilon_1 \bar{E}_1 = \epsilon_2 \bar{E}_2$ . Solving Poisson's equation on each side of the junction will yield the total depletion width and junction capacitance. Sze has given a thorough treatment of this case [17].

For the abrupt p-n junction approximation, assuming total ionization of impurities and neglecting interface states, this yields

$$C = \left[ \frac{q N_{A1} N_{D2} \epsilon_1 \epsilon_2}{2 (\epsilon_1 N_{A1} + \epsilon_2 N_{D2})(V_b - V)} \right]^{\frac{1}{2}}, \quad (2-2)$$

where  $N_{A1}$  = acceptor concentration in semiconductor 1,

$N_{D2}$  = donor concentration in semiconductor 2,

$\epsilon_i$  = electrical permittivity of semiconductor  $i$ ,

$V_b$  = built-in potential,  $V_{b1} + V_{b2}$  for heterojunction,

$V$  = bias voltage.



For  $\epsilon_1 = \epsilon_2$  this expression reduces to the form commonly used for abrupt homojunctions.

Due to the band discontinuities,  $E_c$  and  $E_v$ , the magnitude of the potential barrier as seen by each of the two carrier types is in general different. For this reason, the current through a heterojunction primarily consists of one carrier type. The presence of interface states will cause additional modification to the band structure. Carriers that pass through these states and that are trapped by these states add complications to theoretical predictions.

In attempts at describing heterojunctions by a generalization of homojunction theory, I-V characteristics were expected to be of the form

$$I \propto \exp[qV/\eta kT].$$

This temperature dependence, however, does not agree with experiment. An empirical expression found by Newman,

$$I \propto \exp[V/V_0] \exp[T/T_0],$$

where  $V_0$  and  $T_0$  are constants, seems to be satisfactory for a wide variety of heterojunctions tested. The I-V characteristic of many isotype heterojunctions appears to be that of two back to back diodes. Some of the features of current transport phenomena in heterojunctions are speculated to be due to interband tunneling through interface states or intraband tunneling through band discontinuities.



To this point, the discussion has been limited to single heterojunctions (SH). The I-V characteristics for double heterojunctions (DH) are of progressively greater complexity. For this reason applications taking advantage of optical rather than electrical characteristics seem more obvious at the present time.

#### 4. Electro-Optic Interest in Heterojunctions

Three semiconductor devices whose performance could be improved by the addition of heterostructure are the solar cells, the photodetectors, and the diode injection lasers.

The "window effect" can be used advantageously in both solar cells and detectors [18, 19]. For homojunction photodetector diodes the surface layer, whether n-type or p-type, must be thin (on the order of a penetration depth) in order to absorb as much radiation as possible within a diffusion length of the depletion region. This thin surface layer is highly susceptible to damage in fabrication and deterioration in operation. Attaching contacts to this surface is difficult and often results in loss resistance.

The window effect involves fabricating the surface layer from a larger energy gap semiconductor than the other layer or layers. The surface layer will have negligible absorption for photons of energies less than its band gap. This layer can then be made thicker, increasing mechanical reliability, and more highly doped, reducing series resistance. A third advantage is a result of the refractive index being lower for larger energy gap materials. This provides a more



gradual change in refractive index, i.e., from the air, through the large gap material, to the narrow gap material. Reflection losses are thereby reduced resulting in increased collection efficiency.

For detectors, two additional advantages may be realized by using heterostructure. First, since there will be no response for photons of energies less than the band gap of the narrow energy gap material due to no interband absorption, and no response for photons of energies greater than the band gap of the large gap surface layer due to absorption before reaching the depletion region, a bandpass response is achieved. The passband may be tailored by the selection of the wide and narrow gap materials. Secondly, experiment indicates that larger values of zero-bias resistance are obtainable with heterojunction diodes than with homojunctions [20]. Theoretically, it has been shown that responsivity and detectivity of photovoltaic detectors will increase with increased zero-bias resistance [6]. Also, large zero-bias resistances are necessary to minimize dark current if a photovoltaic detector is to be operated in the fast reverse-biased mode.

Improvements in diode laser operation by the use of heterostructure are the result of both the better confinement of injected carriers to the active region, and better confinement of photons in the active lasing region. The sections to follow are further development of these ideas.



## C. THEORY OF SEMICONDUCTOR INJECTION LASERS

### 1. Principles of Operation

A very lucid qualitative discussion of injection laser fundamentals has been given by Panish and Hayashi [21]. More thorough discussions are given by Sze [17] and Adams and Landsberg [22]. The following treatment is primarily from Sze. This discussion is for the two-level system originally discussed by Einstein in 1917.

The gain in a two-level system is determined by considering the interaction of an atom with a black body radiation field. These considerations yield

$$(W_{12})_{\text{stim}} = B_{12} \rho(\nu), \quad (2-3a)$$

$$(W_{21})_{\text{stim}} = B_{21} \rho(\nu), \quad (2-3b)$$

$$B_{21} = \frac{(c/n)^3}{8\pi h \nu^3 \tau \Delta \nu}, \quad (2-3c)$$

$$B_{12} = \frac{g_2}{g_1} B_{21}, \quad (2-3d)$$

$$\frac{dI_\nu}{dz} = h\nu \left[ (W_{21})_{\text{stim}} N_2 - (W_{12})_{\text{stim}} N_1 \right], \quad (2-3e)$$

where

$(W_{12})_{\text{stim}}$  = stimulated transition rate from level 1 to 2,

$(W_{21})_{\text{stim}}$  = stimulated transition rate from level 2 to 1,

$\rho(\nu)$  = energy density at frequency  $\nu$ ,

\

c = speed of light in vacuum,

n = refractive index of medium,

$\tau$  = spontaneous recombination time,

$\Delta\nu$  = spontaneous emission linewidth,

$g_i$  = degeneracy of level i,

$N_i$  = population density of carriers in level i

that make radiative recombinations,

$I_v = I_o e^{\frac{g(v) z}{\Delta\nu \tau}} = p(v) c/n =$  optical energy flux  
in the z-direction at frequency  $v$ ,

$g(v)$  = optical gain or amplification factor,

and  $B_{12}$  and  $B_{21}$  are stimulated transition constants.

Combining equations (2-3), one can solve for the  
gain,

$$g(v) = \frac{c^2 (N_2 - g_2/g_1 N_1)}{8\pi v^2 n^2 \Delta\nu \tau} . \quad (2-4)$$

From equation (2-4) it can be seen that for positive gain,  
a necessary condition is  $N_2/g_2 > N_1/g_1$ . This condition is  
known as population inversion. The degree of inversion  
can be expressed in terms of a demerit factor defined by

$$\zeta = \left(1 - \frac{N_1 g_1}{N_2 g_2}\right) , \quad (2-5)$$

which is equal to one for perfect inversion and less than  
one in other cases. Equation (2-4) can now be written,

$$g(v) = \frac{c^2 N_2 \zeta}{8\pi v^2 n^2 \Delta\nu \tau} . \quad (2-6)$$



$N_2$  is the population density of carriers in level 2 that make radiative recombinations. To achieve the threshold of population inversion, the injection rate of carriers making radiative recombinations must be equal to the rate at which these carriers recombine, i.e.,

$$\frac{\eta_{int} I_{th}}{q} = \frac{N_2 V}{\tau} \quad , \quad (2-7)$$

where  $\eta_{int}$  = the fraction of injected carriers that recombine radiatively,

$I_{th}$  = threshold current,

$V$  = volume of inverted region.

The geometry of the device is shown in figure (2-2a).

The volume of the inverted region,  $V$ , is equal to the product of the length,  $L$ , the width,  $W$ , and a thickness  $d$  in which the carriers recombine. For the case of no additional carrier confinement this thickness would extend a diffusion length on each side of the junction [16]. This is not consistent with the thickness used by Adams and Landsberg [22], which is the penetration depth of electromagnetic radiation rather than diffusion length. By the implementation of heterostructure, the thickness of the recombination region may be reduced [16]. This is a result of the potential barriers in the conduction and valence bands due to the band discontinuities associated with a heterojunction.



Equations (2-6) and (2-7) may be used to solve for the threshold current density as a function of optical gain,

$$J_{th} = \frac{8\pi q \nu^2 n^2 \Delta\nu d}{c^2 \eta_{int} \zeta} \cdot g(\nu) . \quad (2-8)$$

## 2. Three Layer Dielectric Waveguide Model

An injection laser has an active region, where the population is inverted, sandwiched between two absorbing passive regions. To obtain net gain in an optical cavity, hence lasing, the losses due to fields being supported in the active and passive regions, must be less than the gain due to population inversion in the active region. Anderson has solved for the net gain (or loss) of a junction laser by using a three-layered dielectric model [23]. A standard perturbation approach is used wherein the fields are determined by the real parts of the dielectric constants and then the loss or gain associated with these field distributions is found by considering the imaginary part of the dielectric constant. The error introduced by using only the real part of the dielectric constant in the determination of the field distributions has been shown by Anderson to result in a slightly conservative estimate of mode confinement.

The development to follow will be for a guided TE mode for this is the dominant mode observed in narrow-gap diode lasers [2]. Similar solutions exist for the TM modes. The electric field distribution geometry for TE modes is



is shown in figure (2-2d), from which the transverse propagation constants  $r$ ,  $q$ , and  $p$ , may be defined. Waves are assumed to propagate in the  $z$ -direction as  $e^{(j\omega t - \gamma z)}$  and  $\beta_0 = 2\pi/\lambda_0$  is the free space phase constant.

The electric field in the three regions is given by

$$E_1 = A e^{-px} e^{(j\omega t - \gamma z)}, \quad (2-9a)$$

$$E_2 = \cos(qx + \phi) e^{(j\omega t - \gamma z)}, \quad (2-9b)$$

$$E_3 = B e^{-rx} e^{(j\omega t - \gamma z)}. \quad (2-9c)$$

Neglecting gain or loss in the three layers, the wave equation, equation (1-2), gives

$$\gamma^2 + p^2 + \beta_0^2 \epsilon'_1 = 0, \quad (2-10a)$$

$$\gamma^2 - q^2 + \beta_0^2 \epsilon'_2 = 0, \quad (2-10b)$$

$$\gamma^2 + r^2 + \beta_0^2 \epsilon'_3 = 0. \quad (2-10c)$$

Continuity of the fields across the boundaries requires

$$\tan q_d = \frac{p/q_r + r/q_r}{1 - (p/q_r)(r/q_r)}, \quad (2-11a)$$

$$\tan z\phi = \frac{p/q_r - r/q_r}{1 + (p/q_r)(r/q_r)}. \quad (2-11b)$$



For a generalized solution, Anderson found the following normalization convenient.

$$D \equiv \sqrt{\epsilon_2' - \epsilon_1'} \beta_0 d , \quad (2-12a)$$

$$Q \equiv \frac{\gamma}{\sqrt{\epsilon_2' - \epsilon_1'} \beta_0} , \quad (2-12b)$$

$$P \equiv \frac{r}{\sqrt{\epsilon_2' - \epsilon_1'} \beta_0} , \quad (2-12c)$$

$$R \equiv \frac{r}{\sqrt{\epsilon_2' - \epsilon_3'} \beta_0} , \quad (2-12d)$$

$$\eta \equiv \frac{\epsilon_2' - \epsilon_1'}{\epsilon_2' - \epsilon_3'} , \quad (2-12e)$$

where  $\gamma$  is an asymmetry constant and the regions are always numbered such that  $\epsilon_1' \geq \epsilon_3'$ , so that  $1 \leq \eta \leq \infty$ .

Normalizing equations (2-10) and (2-11), it can be shown that

$$Q = \left[ \frac{\sin^2 QD}{1 + 1/\eta - (2/\sqrt{\eta}) \cos QD} \right]^{1/2} , \quad (2-13a)$$

$$P = \sqrt{1 - Q^2} , \quad (2-13b)$$

$$R = \sqrt{\eta - Q^2} , \quad (2-13c)$$

$$A = Q e^{PD/2} , \quad (2-13d)$$

$$B = \frac{Q}{\sqrt{\eta}} e^{RD/2} , \quad (2-13e)$$



$$\phi = \frac{1}{2} \cos^{-1} \left[ \frac{Q^2}{\sqrt{\eta}} \left( 1 + \frac{PR}{Q^2} \right) \right] . \quad (2-13f)$$

For finite losses, i.e., exponential decay in regions 1 and 3, it can be seen that the necessary requirements are

$$\epsilon'_2 > \epsilon'_1, \epsilon'_3 , \quad (2-14a)$$

$$D > \tan^{-1}(\sqrt{\eta - 1}) . \quad (2-14b)$$

Equation (2-13a) was solved numerically for  $Q$ , for the first order TE mode, assuming several values of  $\eta$ .  $P$  and  $R$  were then determined directly from equations (2-13b) and (2-13c). These solutions are plotted in figures (2-3) and (2-5). The increase in the normalized transverse propagation constants in regions 1 and 3 with increasing normalized thickness indicates improved confinement for wider middle layers.

Anderson solves for the time average power dissipation and the time average energy stored in the three regions by the relations

$$P = \frac{\sigma}{2} \int_{x_1}^{x_2} E^2 dx , \quad (2-15a)$$

$$U = \frac{\epsilon' \epsilon_0}{2} \int_{x_1}^{x_2} E^2 dx , \quad (2-15b)$$



yielding

$$P_1 = \frac{\sigma_1 A^2}{4 \rho} e^{-\rho d}, \quad (2-16a)$$

$$P_2 = \frac{\sigma_2}{4} \left[ d + \frac{\cos 2\phi \sin qd}{q} \right], \quad (2-16b)$$

$$P_3 = \frac{\sigma_3 B^2}{4 r} e^{-r d}, \quad (2-16c)$$

$$U_1 = \frac{\epsilon'_1 \epsilon_0 A^2}{4 \rho} e^{-\rho d}, \quad (2-16d)$$

$$U_2 = \frac{\epsilon'_2 \epsilon_0}{4} \left[ d + \frac{\cos 2\phi \sin qd}{q} \right], \quad (2-16e)$$

$$U_3 = \frac{\epsilon'_3 \epsilon_0 B^2}{4 r} e^{-r d}. \quad (2-16f)$$

Using the relations between electrical and optical constants discussed in section I-B-1,  $\sigma$  can be replaced by  $\sqrt{\epsilon'} \epsilon_0 c \alpha$ , where  $\alpha$  is the loss per unit length. Attenuation is given by energy loss per unit length divided by total energy stored. Therefore, the waveguide attenuation is

$$\alpha_0 = \frac{P_1 \sqrt{\epsilon'_1} / c + P_2 \sqrt{\epsilon'_2} / c + P_3 \sqrt{\epsilon'_3} / c}{U_1 + U_2 + U_3}, \quad (2-17a)$$

$$\text{or } \alpha_0 = \frac{F_1 \alpha_1 + F_2 \alpha_2 + F_3 \alpha_3}{F_1 + F_2 + F_3}, \quad (2-17b)$$

where  $F_1 = \frac{\epsilon'_1}{\epsilon'_2} \left( \frac{1}{f} \right)$ ,

$$F_2 = 1,$$



$$F_3 = \frac{\epsilon'_3}{\epsilon'_2} \left( \frac{P}{\eta R_f} \right) ,$$

and

$$f = \frac{PD}{Q^2} + \frac{P}{Q\sqrt{\eta}} \left( 1 + \frac{PR}{Q^2} \right) \sin QD .$$

To attain the lasing threshold, net waveguide attenuation must be reduced to zero by sufficient gain in the active middle layer. To account for active region gain,  $\alpha_2$  can be replaced by  $(\alpha_2 - g)$  in equation (2-17b). Solving for threshold gain yields

$$g = F_1 \alpha_1 + \alpha_2 + F_3 \alpha_3 . \quad (2-18)$$

Since the population of the active middle layer is inverted and the band gaps of the passive outside layers are made large to provide the optical confining refractive index discontinuity, interband absorption is neglected. The attenuation of each region is, then, the sum of the free carrier absorption and reflection losses through the cleaved facets. This may be written as

$$\alpha = \alpha_{fc} + \frac{1}{2L} \ln \frac{1}{R_1 R_2} , \quad (2-19a)$$

where  $R_1$  and  $R_2$  are the reflectances of the cleaved ends of the cavity. For  $R_1 = R_2 = R$

$$\alpha = \alpha_{fc} + \frac{1}{L} \ln \frac{1}{R} , \quad (2-19b)$$



where

$$R \cong \left(\frac{n-1}{n+1}\right)^2.$$

The threshold gain may now be written

$$g = F_1(\alpha_{FC1} + \frac{1}{L} \ln \frac{1}{R_1}) + \alpha_{FC2} + \frac{1}{L} \ln \frac{1}{R_2} + F_3(\alpha_{FC3} + \frac{1}{L} \ln \frac{1}{R_3}), \quad (2-20)$$

The factors  $F_1$  and  $F_3$ , by which the losses in the passive regions are multiplied, are plotted versus normalized middle layer thickness in figures (2-6) and (2-7). The proportion of loss that takes place in the outside layers decreases rapidly with increasing thickness of the middle layer.

### 3. Design Equations

Evaluation of laser operation is made in this thesis by a study of the effects of various parameters on threshold current, external quantum efficiency, and optical power. Threshold current is determined from equation (2-8), where  $J_{th}$  is given as a function of gain, and equations (2-20), where gain is given in terms of optical constants.

External quantum efficiency, often referred to as differential quantum efficiency, is equal to the internal quantum efficiency multiplied by the loss through the emitting facets divided by total loss.

$$\eta_{ext} = \eta_{int} \left[ \frac{1}{1 + \frac{(F_1 \alpha_{FC1} + \alpha_{FC2} + F_3 \alpha_{FC3}) L}{(F_1 \ln \frac{1}{R_1} + \ln \frac{1}{R_2} + F_3 \ln \frac{1}{R_3})}} \right]. \quad (2-21)$$



The total optical power emitted from the laser is given by [2].

$$P = \eta_{ext} L W (J - J_{th}) E_g. \quad (2-22)$$

For practical applications, devices of low threshold current, high external quantum efficiency, and high output power are sought.

#### D. THRESHOLD AND POWER CALCULATIONS

Threshold and power calculations were made for symmetric double heterojunction (DH) 10.6 micron injection lasers operated at 85°K. The temperature was chosen on the basis that it is probably the temperature at the cold-finger of a liquid nitrogen cryostat. Several controllable parameters were varied to provide an understanding of design tradeoffs. These parameters include cavity length, active region thickness, passive region composition, and passive region doping. Calculations were made for three compositions for the outer layers of both  $Pb_{1-x}Sn_xTe$  and  $Pb_{1-y}Sn_ySe$ . They were zero percent, half of the middle layer active region composition, and a composition very close to that of the middle layer such that the refractive index discontinuity approximated that of a homojunction (HJ) laser. The active region compositions were chosen from equations (1-18) and (1-22) to provide 10.6 micron radiation at 85°K, i.e.,  $x=0.18$  and  $y=0.068$ .



A cavity length of  $500\mu$  and width of  $200\mu$  were used except where stated otherwise. This cavity area is typical of that found in the literature [2, 16, 29]. A summary of these calculations can be found in table 2.

### 1. Estimation of Laser Parameters

The threshold and power equations contain several parameters, some of which may be varied by the designer and others which are constants of the materials used. Theoretical calculations of these constants are quite involved and probably not meaningful, due to the lack of other basic information required in these calculations. Their values are primarily empirical values extracted from  $\text{Pb}_{1-x}\text{Sn}_x\text{Te}$  and  $\text{Pb}_{1-y}\text{Sn}_y\text{Se}$  diode laser data published to date. A discussion of each parameter follows.

#### a. Linewidth

The spontaneous linewidth has been measured for  $\text{PbTe}$  [24] and  $\text{Pb}_{1-x}\text{Sn}_x\text{Te}$  [2, 25] diode lasers at various temperatures. Values range from approximately  $1.5kT$  to  $2.5kT$ . For the following calculations  $2kT$  is used.

#### b. Refractive Index

The refractive index used was derived from the empirical relations presented for  $\text{Pb}_{1-x}\text{Sn}_x\text{Te}$  and  $\text{Pb}_{1-y}\text{Sn}_y\text{Se}$  in section I. The refractive index at 10.6 microns as a function of composition is plotted for  $\text{Pb}_{1-y}\text{Sn}_y\text{Se}$  and  $\text{Pb}_{1-x}\text{Sn}_x\text{Te}$  in figures (2-8a) and (2-9a) respectively.



### c. Free Carrier Absorption

The free carrier absorption coefficient for a semiconductor has been given by Moss [8] as

$$\alpha_{FC} = \frac{\lambda^2 q^2}{4\pi^2 c^3 \epsilon_0 n} \left( \frac{N_D}{m_e^{*2} \mu_e} + \frac{N_A}{m_h^{*2} \mu_h} \right), \quad (2-23)$$

where  $\lambda$  = wavelength of radiation =  $10.6 \mu$ ,

$N_D, N_A$  = donor and acceptor concentrations,

$\mu_e, \mu_h$  = electron and hole mobilities,

and  $m_e^*, m_h^*$  = electron and hole conductivity effective masses.

Donor and Acceptor concentrations used in homojunction diode lasers have typically been  $5 \times 10^{17} \text{ cm}^{-3}$  [2].

For DH GaAs-(GaAl)As-GaAs diode lasers the active region has generally been compensated p-type [16]. Compensation increases the degeneracy and hence lowers the threshold injection level. Threshold calculations were made for the case of doping and compensation to  $5 \times 10^{17} \text{ cm}^{-3}$  in all three regions and another case in which the passive outside regions are doped to  $10^{18} \text{ cm}^{-3}$  to reduce series resistance.

A mobility of  $15,000 \text{ cm}^2/\text{v-sec}$  is chosen. This value is typical of  $\text{Pb}_{1-x}\text{Sn}_x\text{Te}$  and  $\text{Pb}_{1-y}\text{Sn}_y\text{Se}$  for the doping and temperature used [26].

The conductivity effective mass is related to the transverse conductivity effective mass,  $m_t$ , by

$$m_c^* = \frac{3m_t}{2 + \sqrt{K}}, \quad (2-24)$$

where  $K = m_1/m_t$  is the anisotropy constant and



$m_l$  = longitudinal mass. The transverse effective mass is related to the density of states effective mass by

$$m_d^* = M_c^{2/3} K^{1/2} m_t. \quad (2-25)$$

For  $Pb_{1-x}Sn_xTe$   $M_c = 4$ ,  $K = 12$ , and  $m_d^* = 1.12 E_g m_0$ , where  $E_g$  is the band gap in eV and  $m_0$  is the mass of an electron, while for  $Pb_{1-y}Sn_ySe$   $M_c = 4$ ,  $K = 2$ , and  $m_d^* = 1.165 E_g m_0$  [26].

A solution for the free carrier absorption of 10.6 micron radiation yields

$$\alpha_{Fc} = 2.52 / (n E_g^2), \quad (2-26a)$$

for  $Pb_{1-x}Sn_xTe$  and

$$\alpha_{Fc} = 1.02 / (n E_g^2), \quad (2-26b)$$

for  $Pb_{1-y}Sn_ySe$ . These equations are plotted as a function of composition in figures (2-8b) and (2-9b) for  $Pb_{1-y}Sn_ySe$  and  $Pb_{1-x}Sn_xTe$  respectively.

#### d. Internal Quantum Efficiency

A wide range of values have been reported for the internal quantum efficiency of narrow-gap laser diodes. Recent experimental results indicate a value on the order of 0.05 for lasers of width greater than 100 microns [27].

#### e. Demerit Factor

A demerit factor has been estimated empirically to account for observed variation of threshold current with temperature as reported by Ralston and others [27].



A change of  $J_{th}$  was observed from  $10^0$ K to  $80^0$ K that could not be accounted for by the following variations: a factor of 2 decrease in diffusion length, a factor of 8 increase in linewidth, and a factor of 2 increase in threshold gain, due to increased significance of free carrier absorption. This additional change was absorbed in the demerit factor. This resulted in a demerit factor of 0.4.

f. Active Region Thickness

The active region thickness in the homojunction laser calculation was assumed to be two diffusion lengths, i.e., 20 microns at  $77^0$ K [28]. For heterojunction calculations, perfect confinement of carriers to the middle semiconductor layer was assumed. This assumption has been made for (GaAl) As-GaAs heterojunctions due to the potential barrier presented by the band discontinuities [16]. The actual extent of carrier confinement in IV-VI alloy narrow-gap junction lasers cannot be estimated, however, until more extensive information is available concerning the electron affinity and work function of these materials.

g. Homojunction Refractive Index Discontinuity

The refractive index discontinuity in a  $Pb_{1-x}Sn_xTe$  diode laser was roughly approximated using the three layered dielectric waveguide model and the "light intensity versus distance perpendicular to junction" data of Ralston and others [27]. The procedure involves fitting the light intensity data with the square of a field



distribution as shown in figure (2-2d). Using the active region thickness estimated by Ralston, approximations were made for transverse propagation constants. Since the transverse propagation constant - middle layer thickness product is equal to the product of the corresponding normalized values, figures (2-3) to (2-5) can be used to determine the normalized thickness corresponding to the calculated product. With knowledge of both the middle layer thickness and its normalized value, the normalization constant may be determined. This constant contains the refractive index discontinuity as shown in equations (2-12).

## 2. Threshold Current

In the threshold current calculations a minimum was observed for an active region thickness,  $d$ , ranging from  $0.5\mu$  to  $1.5\mu$ , depending upon other laser parameters. The explanation for this is that for smaller thickness the  $F_1$  and  $F_3$  factors, which multiply the passive region absorption, become very large. This is equivalent to poor confinement, resulting in a wide field distribution. On the other hand, for a large  $d$ , passive region absorption becomes negligible and threshold current becomes directly proportional to  $d$ .

Lower thresholds were calculated for larger refractive index discontinuities, due to better confinement, hence, smaller regions of population inversion. Lower thresholds were found also for lower levels of doping, because of reduction in the free carrier absorption.



Thresholds were also lower for longer cavities due to greater gain over losses through the cleaved facets.

Threshold current of DH  $\text{Pb}_{1-x}\text{Sn}_x\text{Te}$  diode lasers of a  $500\mu$  cavity length ranged from  $115/\text{cm}^2$  to  $215/\text{cm}^2$  for active region thickness of  $0.6\mu$  to  $1.0\mu$ . These results are plotted in the form of a threshold current as a function of active region thickness in figure (2-10). Homojunction (HJ) calculations resulted in thresholds of approximately  $2500\text{A}/\text{cm}^2$  and  $3700\text{A}/\text{cm}^2$  for semi-conductor dopings of  $5 \times 10^{17} \text{ cm}^{-3}$  and  $10^{18} \text{ cm}^{-3}$ , respectively. This did not take into account the improvement in demerit factor due to increased degeneracy, however.

$\text{Pb}_{1-y}\text{Sn}_y\text{Se}$  DH calculations gave minimum thresholds of  $100\text{A}/\text{cm}^2$  to  $150\text{A}/\text{cm}^2$  for active region thickness of  $0.9$  to  $1.5\mu$ . Results of these calculations are plotted in figure (2-11). HJ thresholds were  $1300\text{A}/\text{cm}^2$  and  $1900\text{A}/\text{cm}^2$  for dopings of  $5 \times 10^{17} \text{ cm}^{-3}$  and  $10^{18} \text{ cm}^{-3}$ , respectively.

Threshold current as a function of active region thickness for various cavity lengths is plotted in figure (2-12) from  $\text{Pb}_{1-x}\text{Sn}_x\text{Te}$  data. Figure (2-15a) displays threshold current as a function of cavity length.

### 3. External Quantum Efficiency

External quantum efficiency for  $\text{Pb}_{1-y}\text{Sn}_y\text{Se}$  is plotted as a function of  $d$  in figure (2-13a) and (2-13b) for passive region doping levels of  $5 \times 10^{17} \text{ cm}^{-3}$  and  $10^{18} \text{ cm}^{-3}$ , respectively. Efficiency decreases with increasing  $d$  for the lower doping levels. It can be seen that this



trend is reversed, however, as the passive region doping is increased. The reason for this is due to the free carrier absorption being proportional to the doping level. When the free carrier absorption coefficient of the active region is greater than that of the passive regions the laser is more efficient if most of the field distribution is located in passive regions. A larger fraction of the field will exist in the passive regions if the active region is made narrower. This situation is simply reversed if the absorption coefficient is larger in the passive regions.

The external quantum efficiencies vs.  $d$  for several  $Pb_{1-x}Sn_xTe$  DH lasers are plotted in figures (2-14a) and (2-14b). Figure (2-14b) is plotted for four cavity lengths. The decrease in external quantum efficiency with length noted in this figure and in figure (2-15b) is a result of a greater proportion of loss occurring through free carrier absorption and less occurring in light emitted as the length of the absorbing cavity is increased. Efficiencies calculated for the HJ lasers are in general lower than for the DH lasers and are listed in table 2.

#### 4. Output Power

Optical output power versus current calculations were made for three  $Pb_{1-x}Sn_xTe$  and three  $Pb_{1-y}Sn_ySe$  diode lasers. All carrier concentrations were assumed to be  $5 \times 10^{17} \text{ cm}^{-3}$ . Diode areas are  $500\mu$  by  $200\mu$  in all cases. The three  $Pb_{1-x}Sn_xTe$  lasers are characterized by passive region compositions of  $x=0$ ,  $x=.09$ , and  $x=0.18$  and are



TABLE 2

THEORETICAL DH LASER CALCULATIONS FOR  $\lambda = 10.6 \mu$  AND  $T = 85^{\circ}\text{K}$ 

$\text{Pb}_{1-x}\text{Sn}_x\text{Te}$			
$x_{1,3}$	$N_{1,3} (\text{cm}^{-3})$	$J_{th} (\text{A/cm}^2)$	$\eta_{ext}$
0	$5 \times 10^{17}$	116	.0232
0	$10^{18}$	137	.0190
.09	$5 \times 10^{17}$	175	.0200
.09	$10^{18}$	216	.0160
Homojunction	$5 \times 10^{17}$	2421	.0163
Homojunction	$10^{18}$	4052	.0097

$\text{Pb}_{1-y}\text{Sn}_y\text{Se}$			
$y_{1,3}$	$N_{1,3} (\text{cm}^{-3})$	$J_{th} (\text{A/cm}^2)$	$\eta_{ext}$
0	$5 \times 10^{17}$	95	.0308
0	$10^{18}$	108	.0268
.034	$5 \times 10^{17}$	132	.0288
.034	$10^{18}$	155	.0246
Homojunction	$5 \times 10^{17}$	1305	.0261
Homojunction	$10^{18}$	1928	.0177



presented on log-log and linear plots in figures (2-16a) and (2-17), respectively. Passive region compositions of the  $\text{Pb}_{1-y}\text{Sn}_y\text{Se}$  lasers are  $y=0$ ,  $y=0.034$ , and  $y=0.068$ . The laser output power versus current characteristics are displayed on log-log and linear plots in figures (2-16b) and (2-18), respectively.

One may note that in all cases more than 3 milliwatts of power can be expected from DH lasers at bias currents less than the threshold of the corresponding HJ laser. It should, therefore, be kept in mind that when threshold currents differ, a direct comparison of external quantum efficiencies may be misleading.

## E. OBSERVATION

### 1. Design Tradeoffs

Injection laser design involves the specification of several parameters. The following is a list of these parameters with some considerations for their optimum selections.

#### a. Composition

The composition of the middle layer active region is determined by the desired lasing wavelength. For outer layer passive regions in a DH or SH laser, choosing the composition to provide the largest possible energy gap is desirable on three counts. First, due to the large refractive index discontinuity, there is a high degree of optical confinement which reduces the injection level



necessary for threshold. Secondly, greater band discontinuities provide increased carrier confinement which also tends to decrease the threshold injection level. Finally, the free carrier absorption in the passive regions is reduced by the inverse square relationship between free carrier absorption and the band gap. However, large band gap differences led to two disadvantages in creating more non-radiative interface states, due to larger lattice mismatch, and limited output power.

The intense optical confinement over a small area can cause faster deterioration of laser performance or even destroy the laser facets. A limit for catastrophic failure of  $10^6 \text{ W/cm}^2$  has been estimated for GaAs diodes [16]. The lasers studied in this thesis could provide sufficient local oscillator power, i.e., a few milliwatts, while maintaining optical flux densities less than the catastrophic failure limit mentioned above by more than two orders of magnitude. Lattice mismatch which resulted from composition variation across the heterojunctions may introduce interface states through which injected carriers recombine non-radiatively. It is not believed that this factor would be as damaging in IV-VI semiconductor diodes, since, lattice parameter mismatch is less than 0.5%, whereas laser action has been reported for Pb-PbTe diodes [24] for which the mismatch is in excess of 20%.

#### b. Carrier Concentration

The primary disadvantage of a high doping level is that the free carrier absorption coefficient is



proportional to the carrier concentration. Advantages in increased carrier concentrations are reduced resistivity in all regions and increased degeneracy in the active region. The increased degeneracy, producing band tails in the active region, was significant to the development of efficient room temperature operation of (GaAl)As heterojunction lasers [16]. It may be advantageous to fabricate thin, lightly doped passive regions, characterized by low free carrier absorption, on a thick, highly doped substrate, characterized by low resistivity [16].

### c. Active Region Thickness

A minimum in threshold current is found for an active region thickness on the order of  $1\mu$  in figures (2-10) through (2-12). Although smaller thickness may increase external quantum efficiency somewhat, as seen in figures (2-18) and (2-14), the tremendous increase in threshold current would necessitate the use of more input power to reach threshold. Also, the higher optical flux densities resulting may damage the laser facets.

Thicker active regions provide increased power capabilities, due to a larger emitting area, at the cost of higher thresholds. For applications requiring higher output power, large optical cavity (LOC) and SH lasers have been fabricated [16]. LOC lasers employ multiple heterojunctions to confine carriers to a thin region within a thicker region of optical confinement. These increased power capabilities would probably not be necessary, however for a laser used as a



local oscillator in the  $\text{CO}_2$  laser system, where milliwatts of power over a  $1\mu$  by  $200\mu$  facet yields optical flux densities on the order of  $10^3 \text{W/cm}^2$ .

Figure (2-12) reveals that the optimum thickness increases with the cavity length.

#### d. Cavity Length

The problem of selecting a cavity length,  $L$ , may best be understood in view of figures (2-15) where threshold current and external quantum efficiency are presented as functions of  $L$ .

Cavity length determines longitudinal mode spacing in accordance with the relation [17],

$$\Delta\lambda = \frac{\lambda^2}{2nL\left(1 - \frac{\lambda}{n} \frac{dn}{d\lambda}\right)} . \quad (2-27)$$

For these lasers, 0.02 to 0.05 cm should be considered, since longer cavity lengths have little effect on reducing the threshold but will introduce more longitudinal modes under the spontaneous recombination linewidth. On the other hand, shorter lengths, less than 0.02 cm, would only increase external quantum efficiency by a factor of two while drastically increasing the threshold current.

#### e. Cavity Width

Optical power is directly proportional to cavity width. Consistent single-frequency, single spacial mode operation has been reported only for thin cavities [27]. It reported that parasitic off-axis bounce modes can



be greatly reduced with widths of  $100\mu$  or less. However, single-frequency mode operation has been reported for cavity widths up to  $250\mu$  [2].

## 2. Present State of Narrow-Gap Laser Operation

As of the time of this writing, CW operation at  $77^0K$  had not been reported for  $Pb_{1-x}Sn_xTe$  or  $Pb_{1-y}Sn_ySe$  injection lasers. A summary of data reported by several groups on achievements in  $Pb_{1-x}Sn_xTe$  diode laser operation is contained in table 3. The most recent improvement of these lasers was the increased external quantum efficiencies obtained using polished, rather than cleaved, end-mirrors [29]. The next breakthrough for narrow-gap lasers may be the implementation of heterostructure.



TABLE 3

STATE OF  $Pb_{1-x}Sn_xTe$  INJECTION LASERS

Remarks	Composition	Mode	$\tau(^{\circ}K)$	$\lambda_0(\mu)$	$J_{th}(A/cm^2)$	$\eta_{int}$	$\eta_{ext}$	$P(mW)$ at $J(A/cm^2)$	References
50 $\mu$ Stripe-Geometry	.12	Pulsed	77	8.8	4100				27
100 $\mu$ "	.12	Pulsed	77	8.8	3300				27
	.15	Pulsed	77	9.5	3000				31
	.2	Pulsed	77	11.2	12500				31
Bi-doped	.26	Pulsed	77	15.5	1400				2
	.12	CW	12	11.3			.05	3.4	500
Lowest threshold reported	.19	CW	12	14.	20	.15	.086		2
	.2	Pulsed	12	15.1	275		.08	100	12000
	.2	CW	12	15.1	275		.05	5	1600
Proton bombardment	0	CW	4.2	6.24	138		.000006	.010	700
" "	.12	CW	4.2	11.					25
50 $\mu$ Stripe-Geometry	.12	Pulsed	4.2	10.9	1170	.013	.005	.9	6900
100 $\mu$ "	.12	Pulsed	4.2	10.9	170	.055	.034		27
Sb-diffused	.15	Pulsed	4.2	10.6	50		.0009		15500
Annealed	.16	Pulsed	4.2	10.6	100		.0085	10	15500
Polished facets	.117	CW	1.9	10.6	300	.3	.16	10.6	1540
" "	.117	CW	1.9	10.6	140	.3	.16	6	960
Temperature tuning	.1	Pulsed	7	9.6					32
" "	.1	Pulsed	85	7.9					32
Schottky barrier	0	Pulsed	12	6.54	240		.01		24



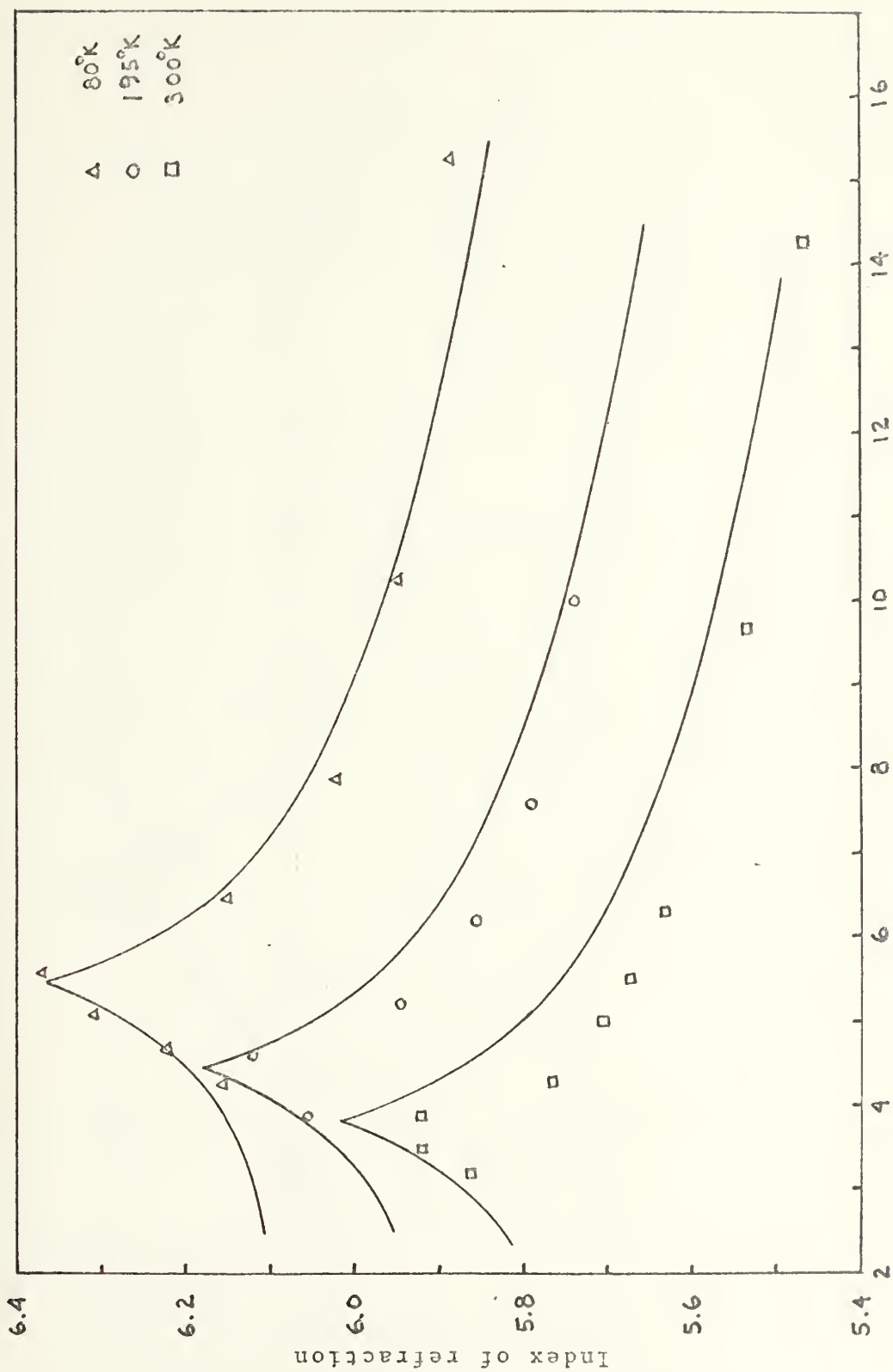


FIGURE 1-1. Wavelength ( $\mu$ ) Index of refraction of PbTe



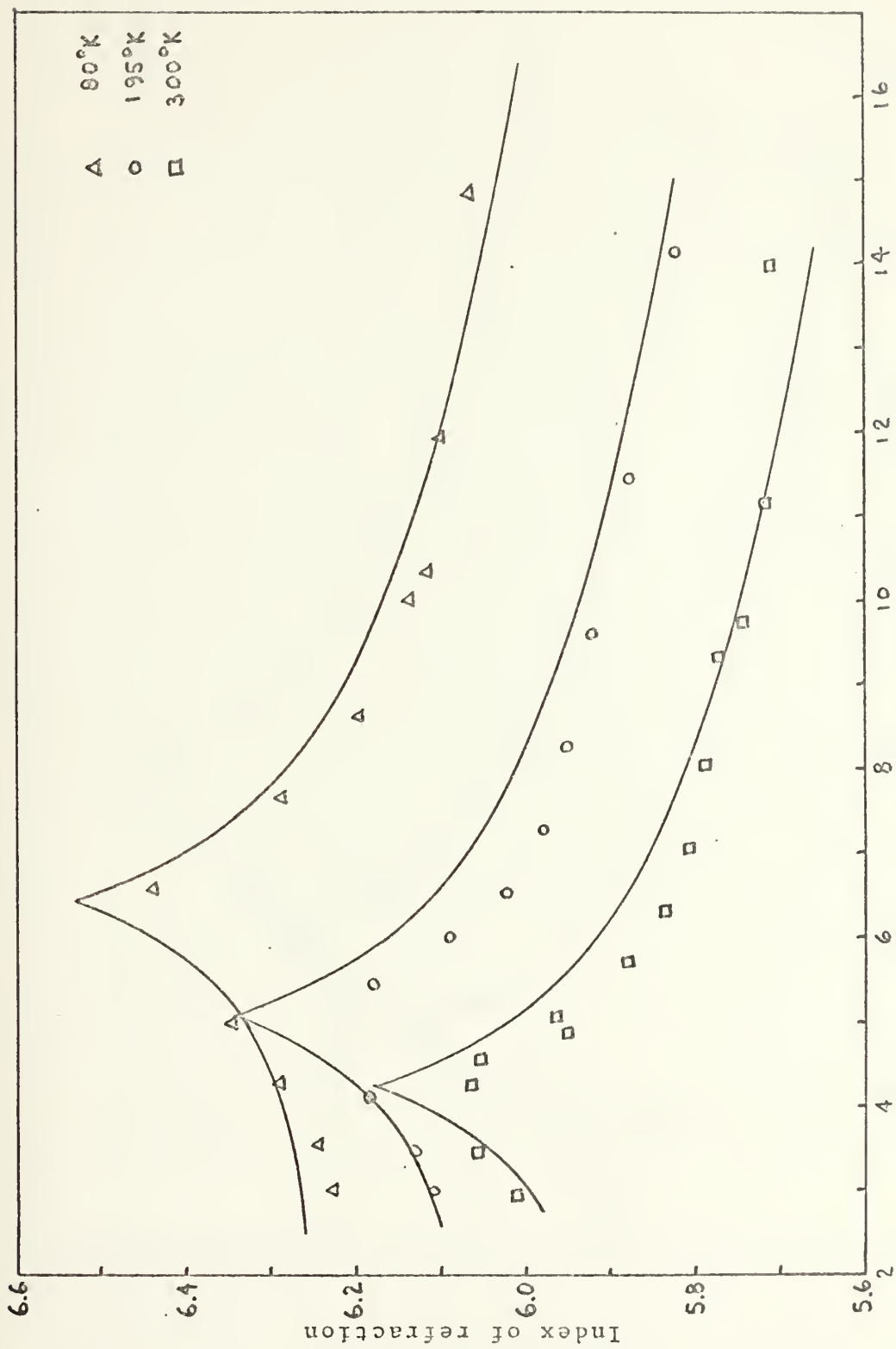


FIGURE 1-2. Index of refraction of  $\text{Pb}_{.94}\text{Sn}_{.06}\text{Te}$



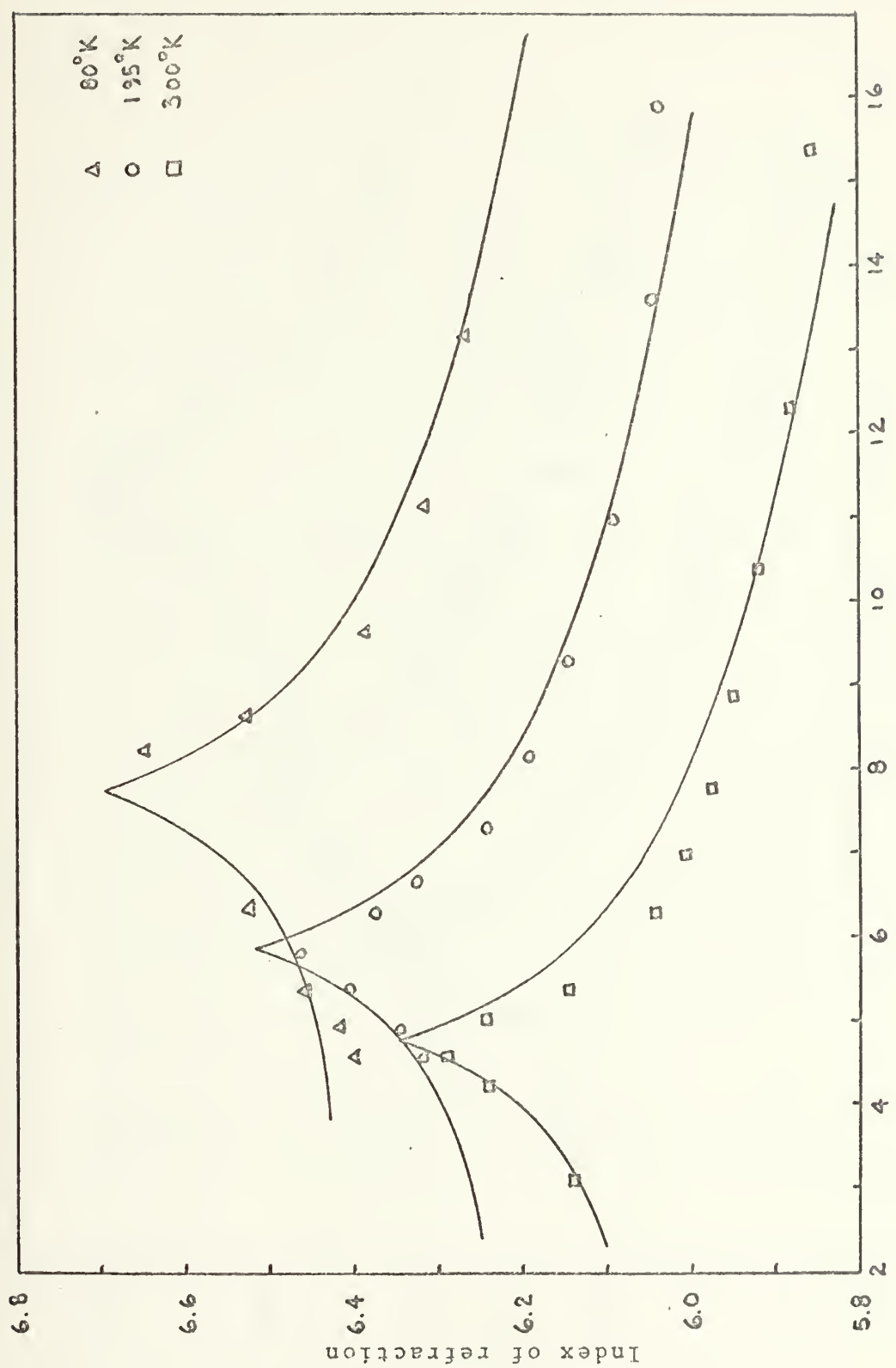


FIGURE 1-3. Index of refraction of Pb.88Sn.12Te  
Wavelength ( $\mu$ )



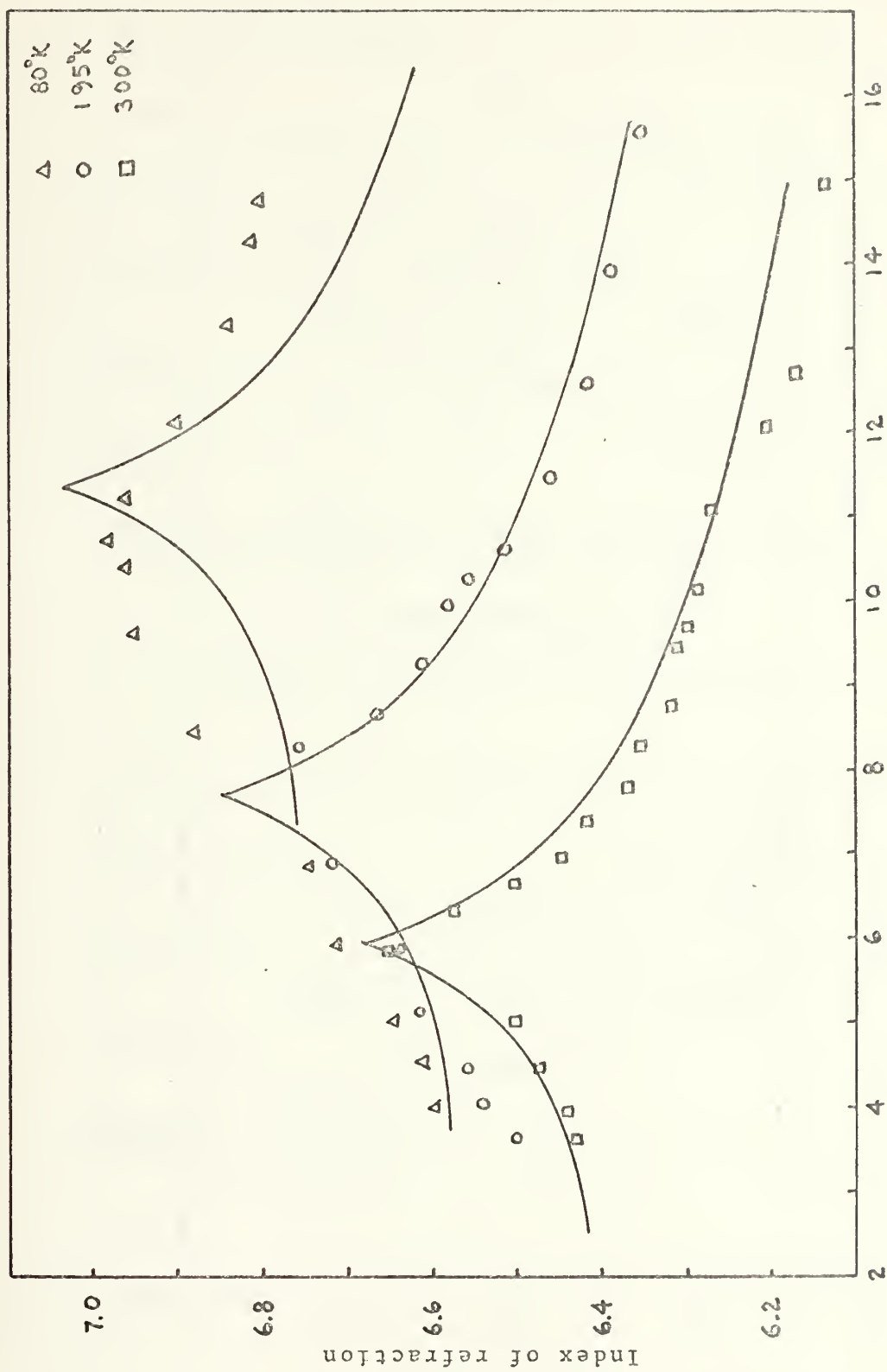


FIGURE 1-4. Index of refraction of  $\text{Pb.76Sn.24Te}$



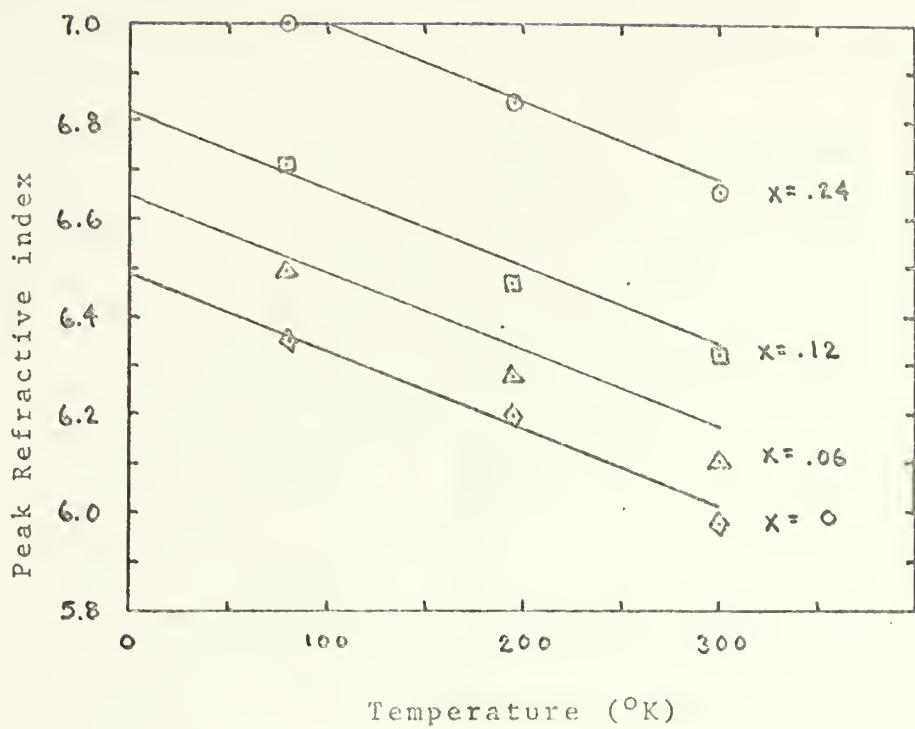


FIGURE 1-5.  $n_p$  vs. T for  $Pb_{1-x}Sn_xTe$

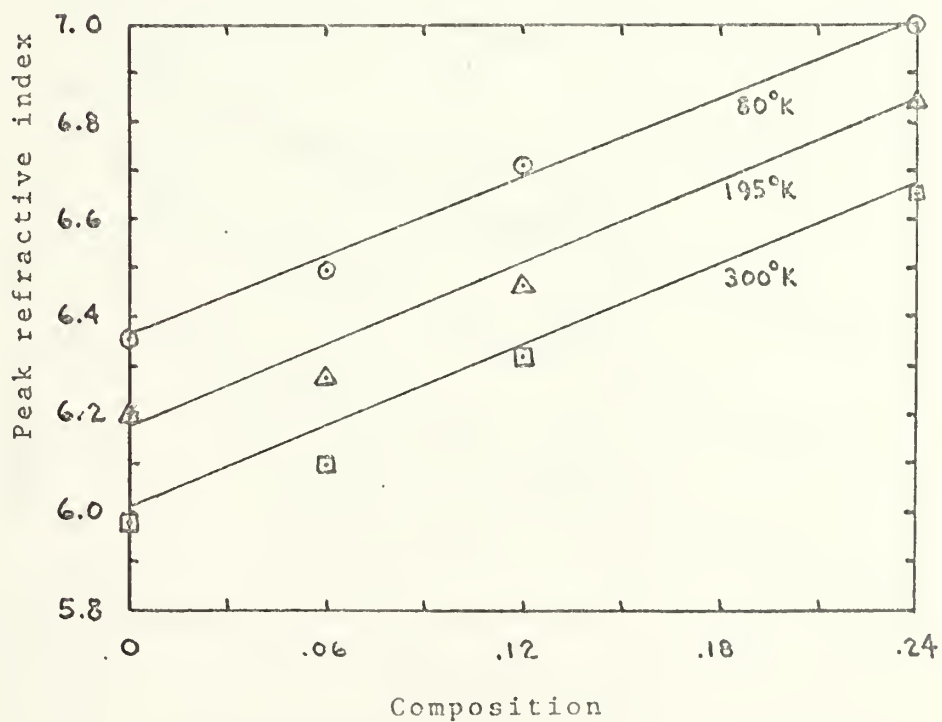


FIGURE 1-6.  $n_p$  vs. x for  $Pb_{1-x}Sn_xTe$



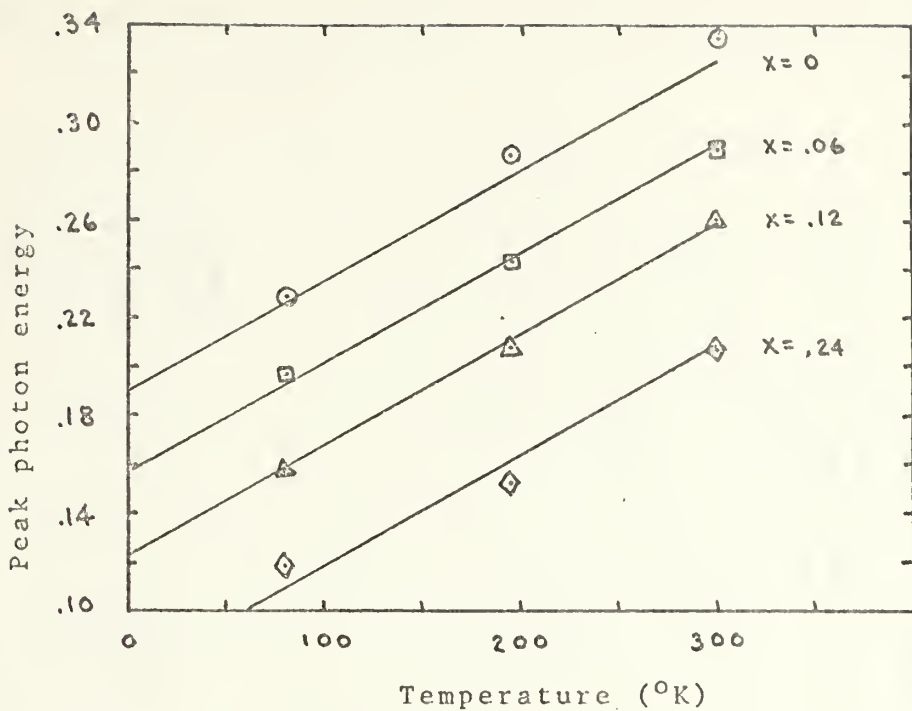


FIGURE 1-7.  $E_p$  vs.  $T$  for  $Pb_{1-x}Sn_xTe$

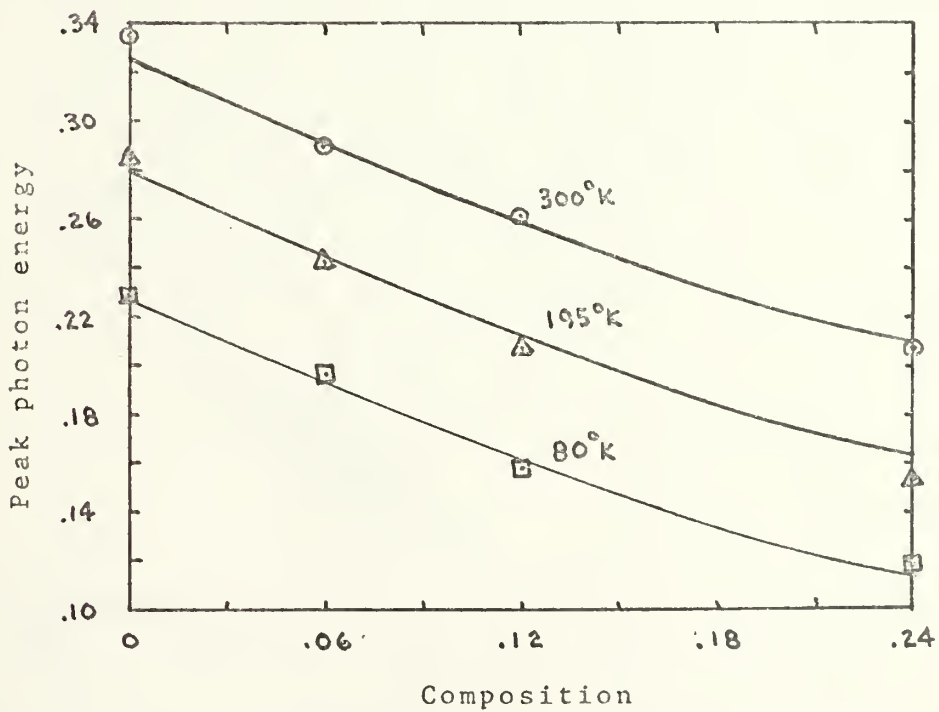


FIGURE 1-8.  $E_p$  vs.  $x$  for  $Pb_{1-x}Sn_xTe$



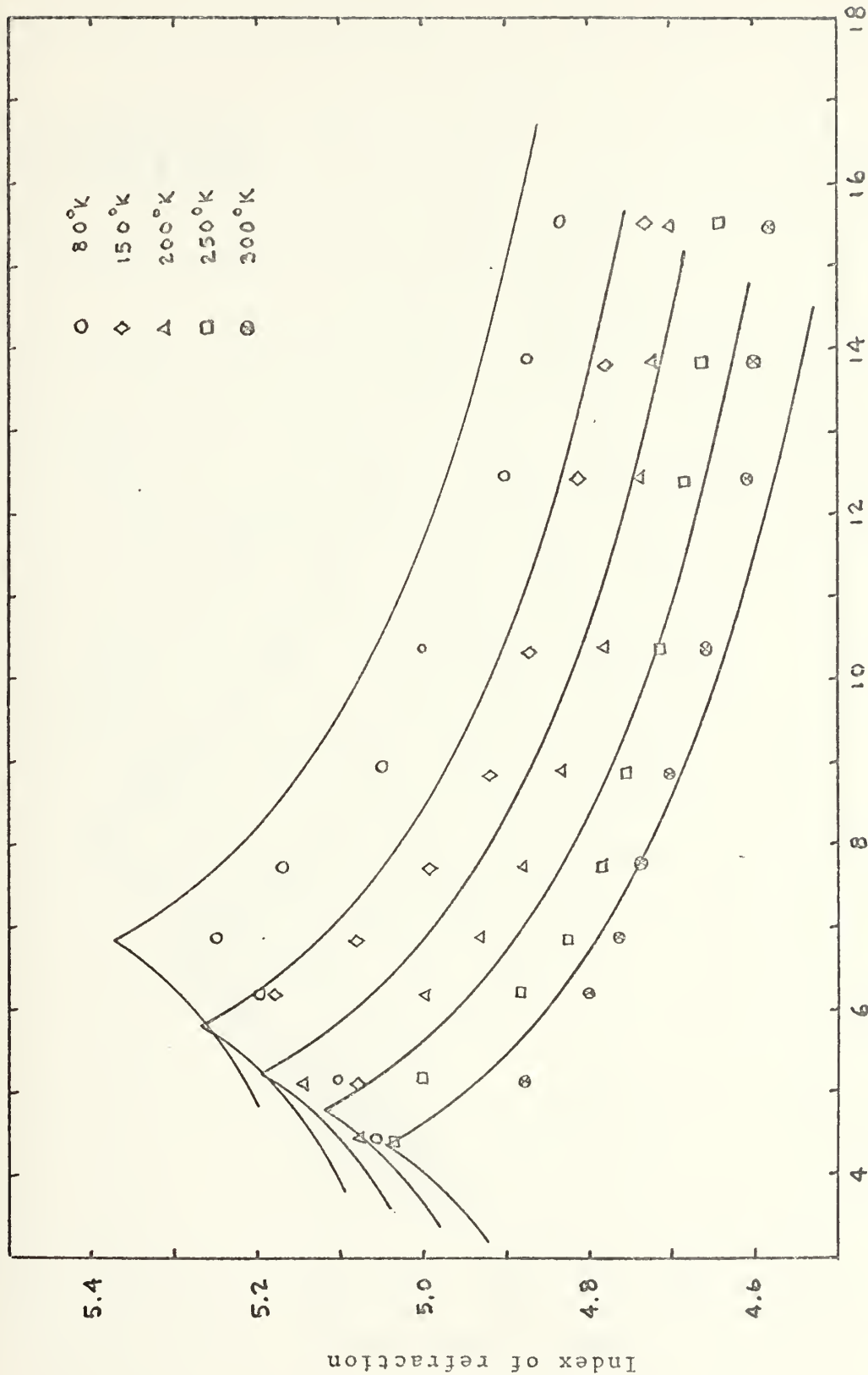


FIGURE 1-9. Index of refraction of Pb Se



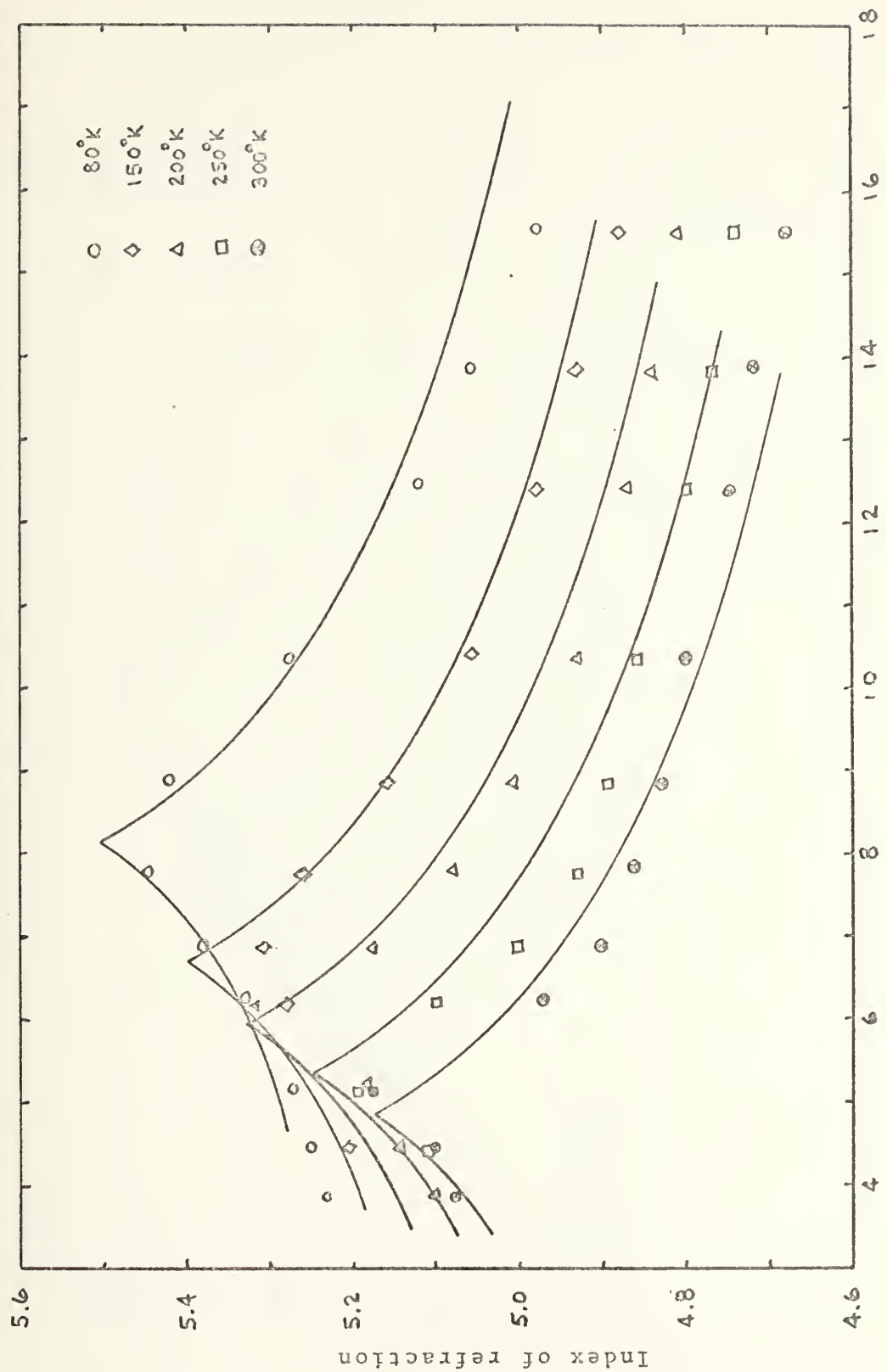


FIGURE 1-10. Index of refraction of Pb.965Sn.035Se



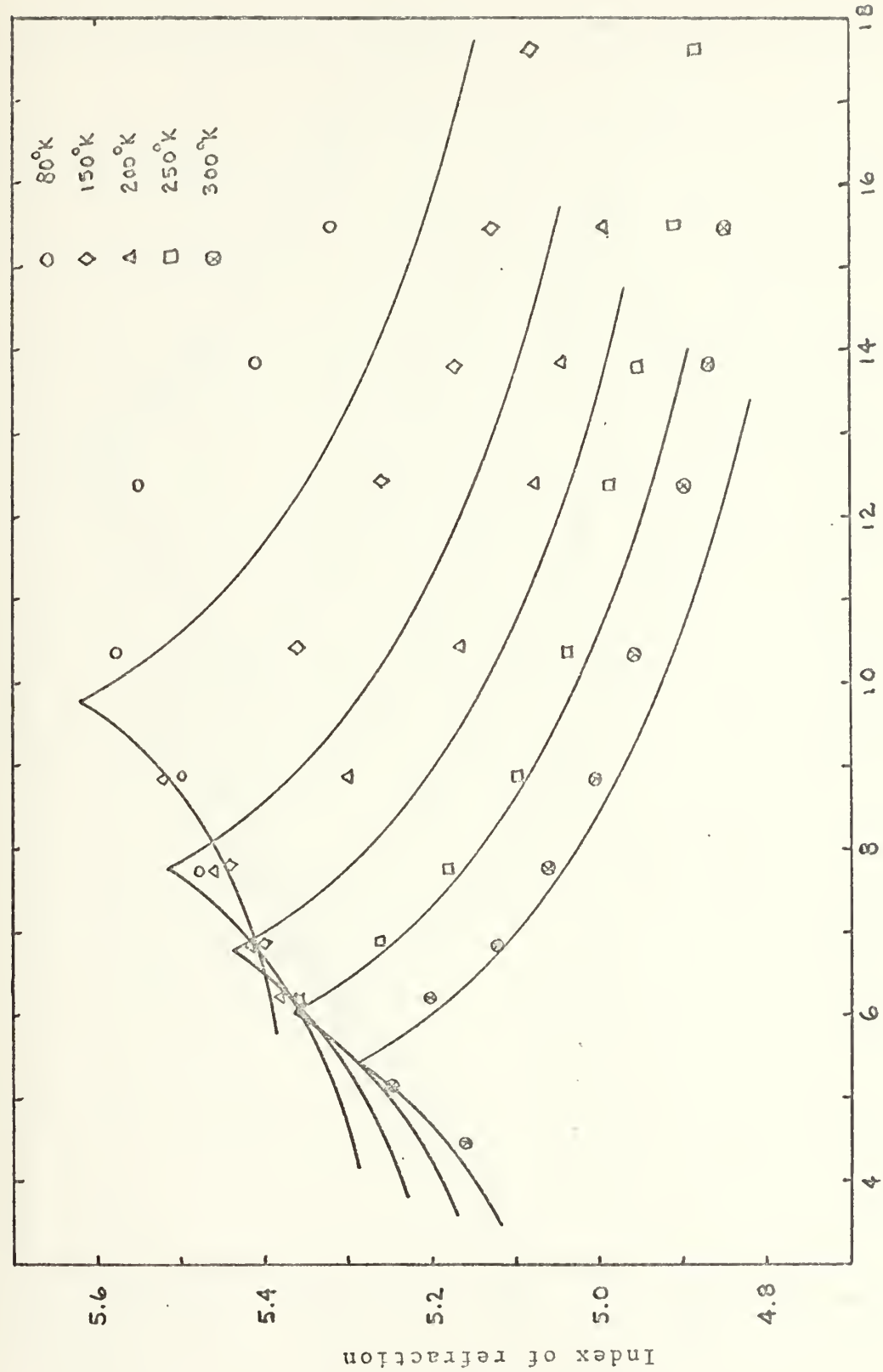
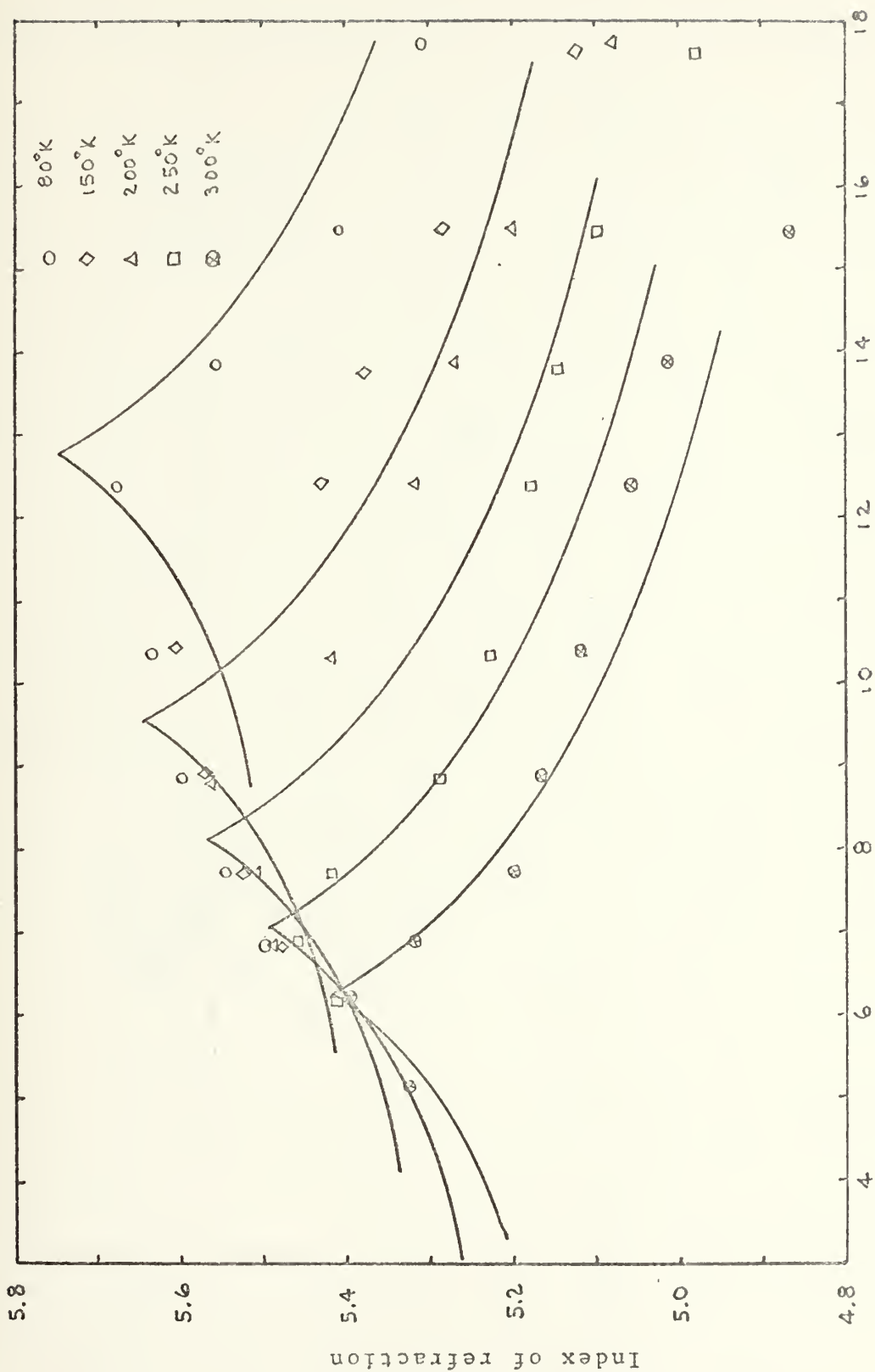


FIGURE 1-11. Index of refraction of Pb.935Sn.065Se  
Wavelength ( $\mu$ )



FIGURE 1-12. Wavelength ( $\mu$ ) Index of refraction of  $\text{Pb}_{0.9}\text{Sn}_{0.1}\text{Se}$





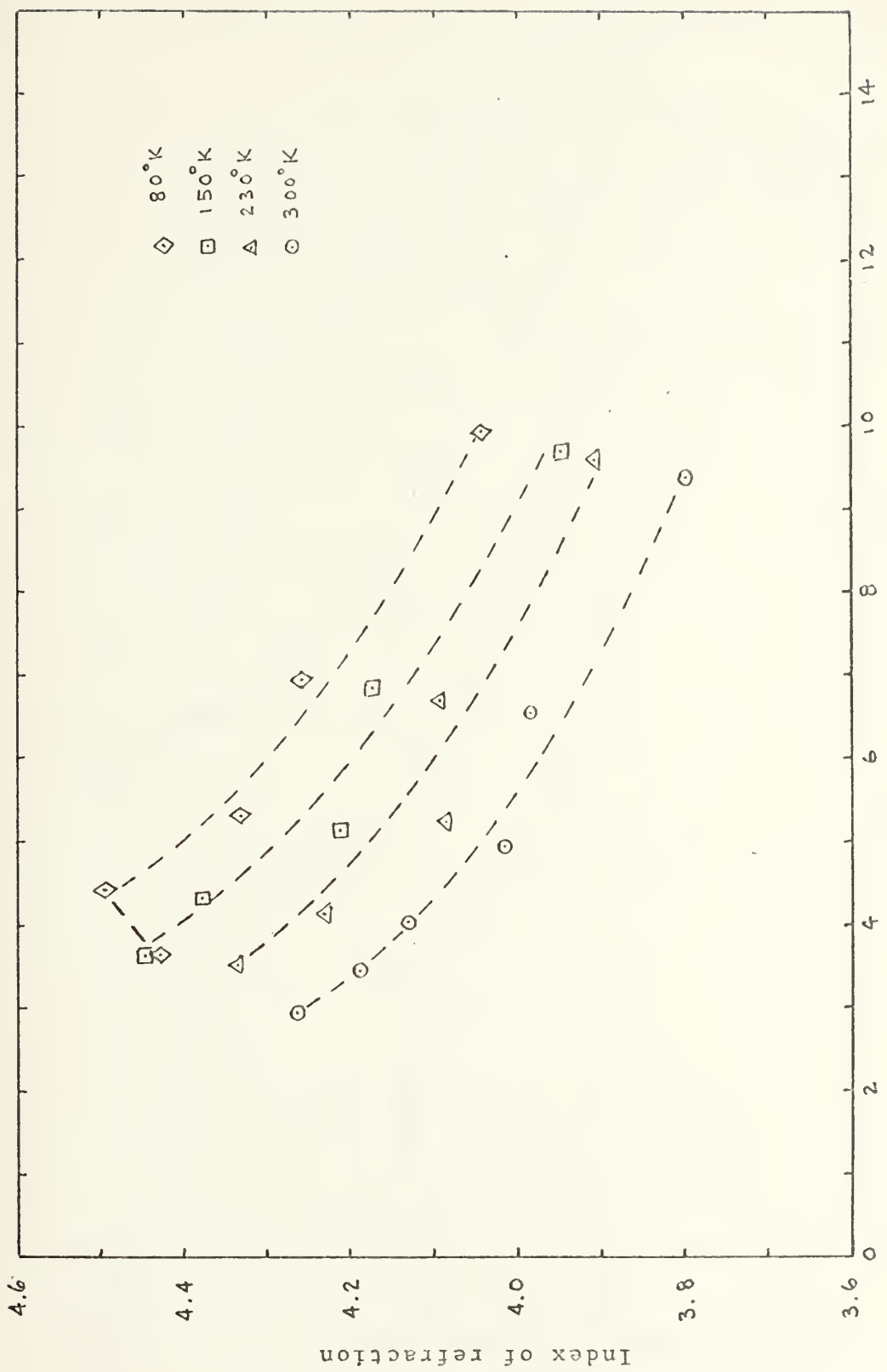


FIGURE 1-13. Index of refraction of  $\text{Pb.8Se.2}$



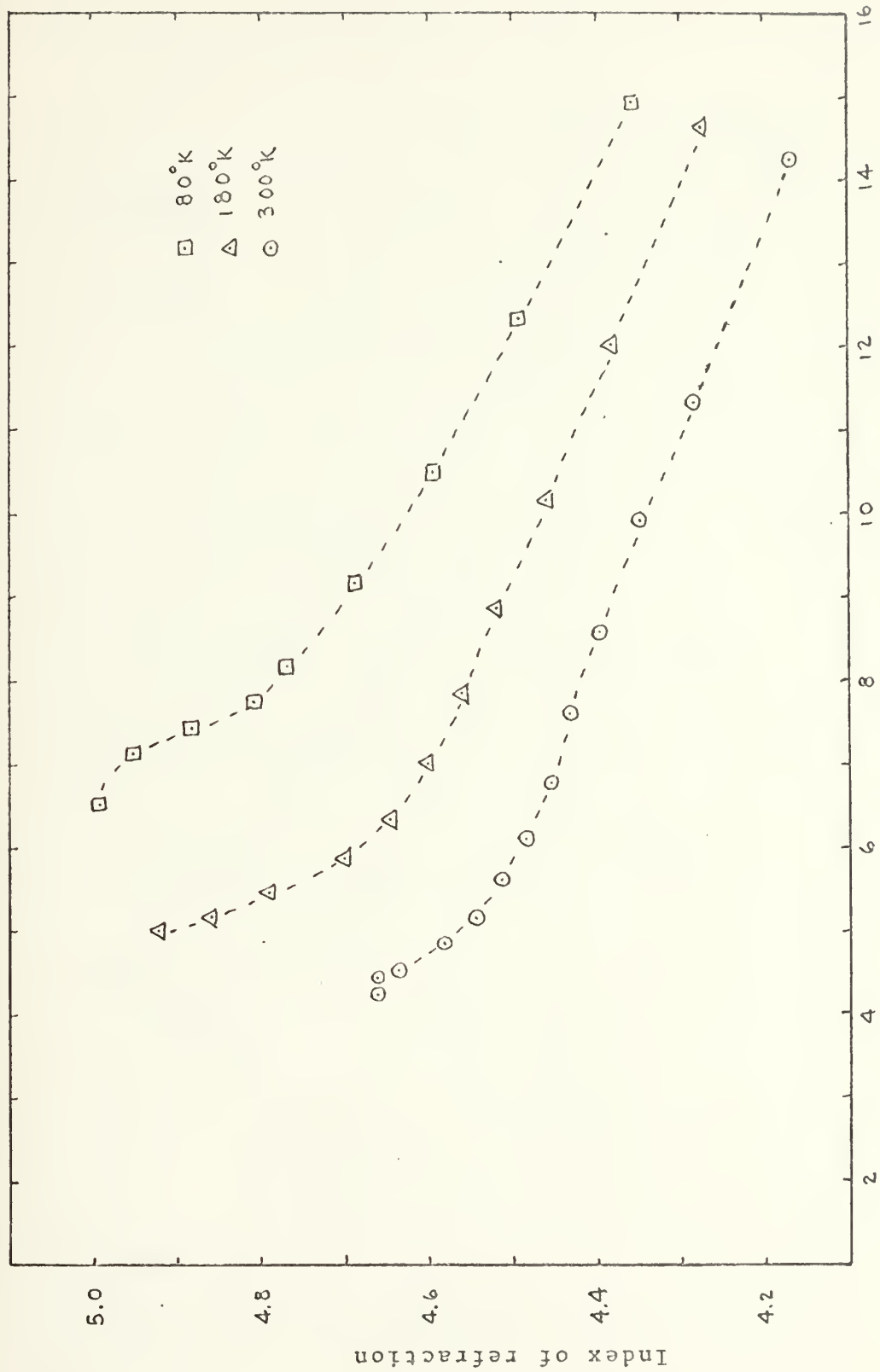


FIGURE 1-14. Index of refraction of  $\text{PbS} \cdot 64\text{Se} \cdot 36$



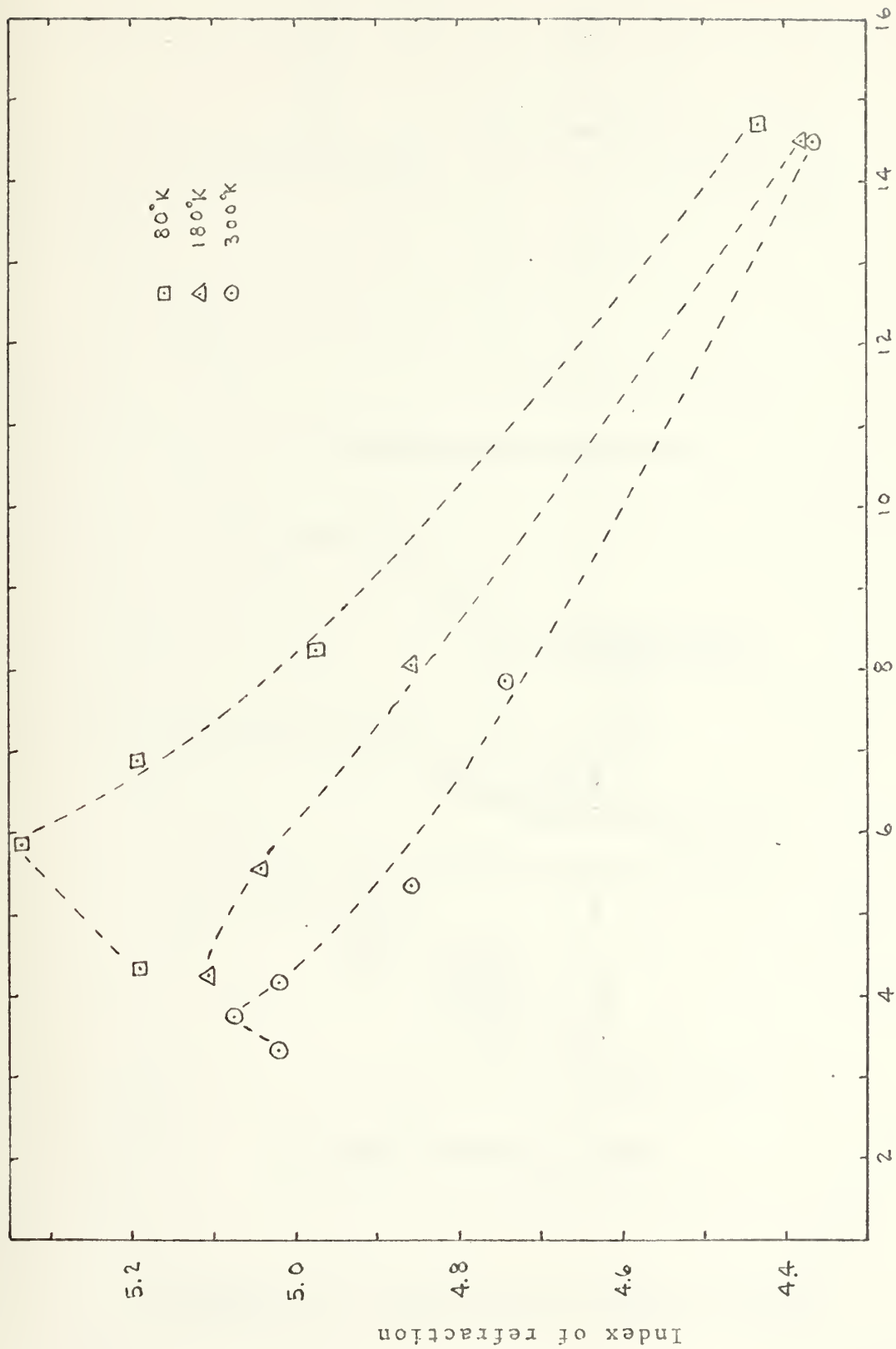
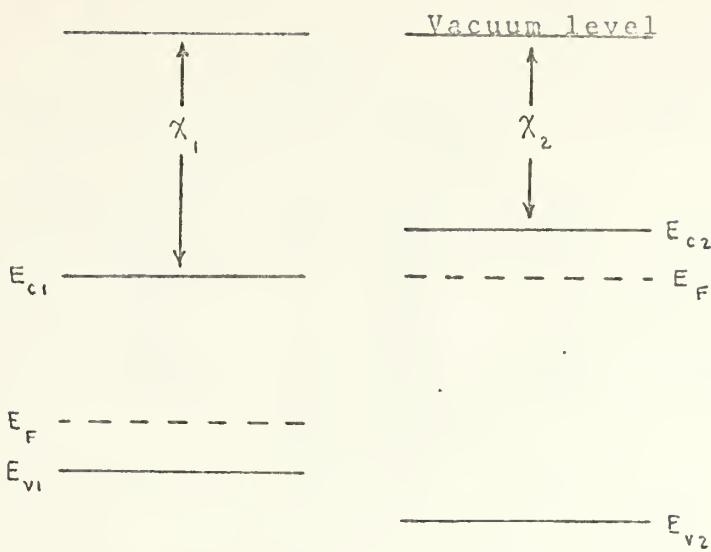
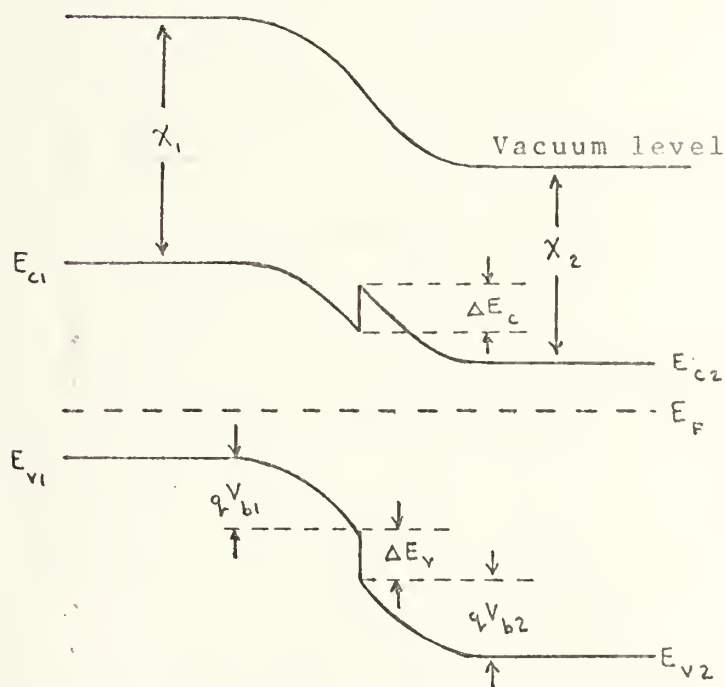


FIGURE 1-15. Wavelength ( $\mu\text{m}$ ) Index of refraction of  $\text{PbS.4Se.6}$





(a) Isolated semiconductors



(b) Ideal heterojunction

FIGURE 2-1. Heterojunction band diagram



(d) Electric field intensity    (c) Refractive index    (b) Band gap    (a) Geometry

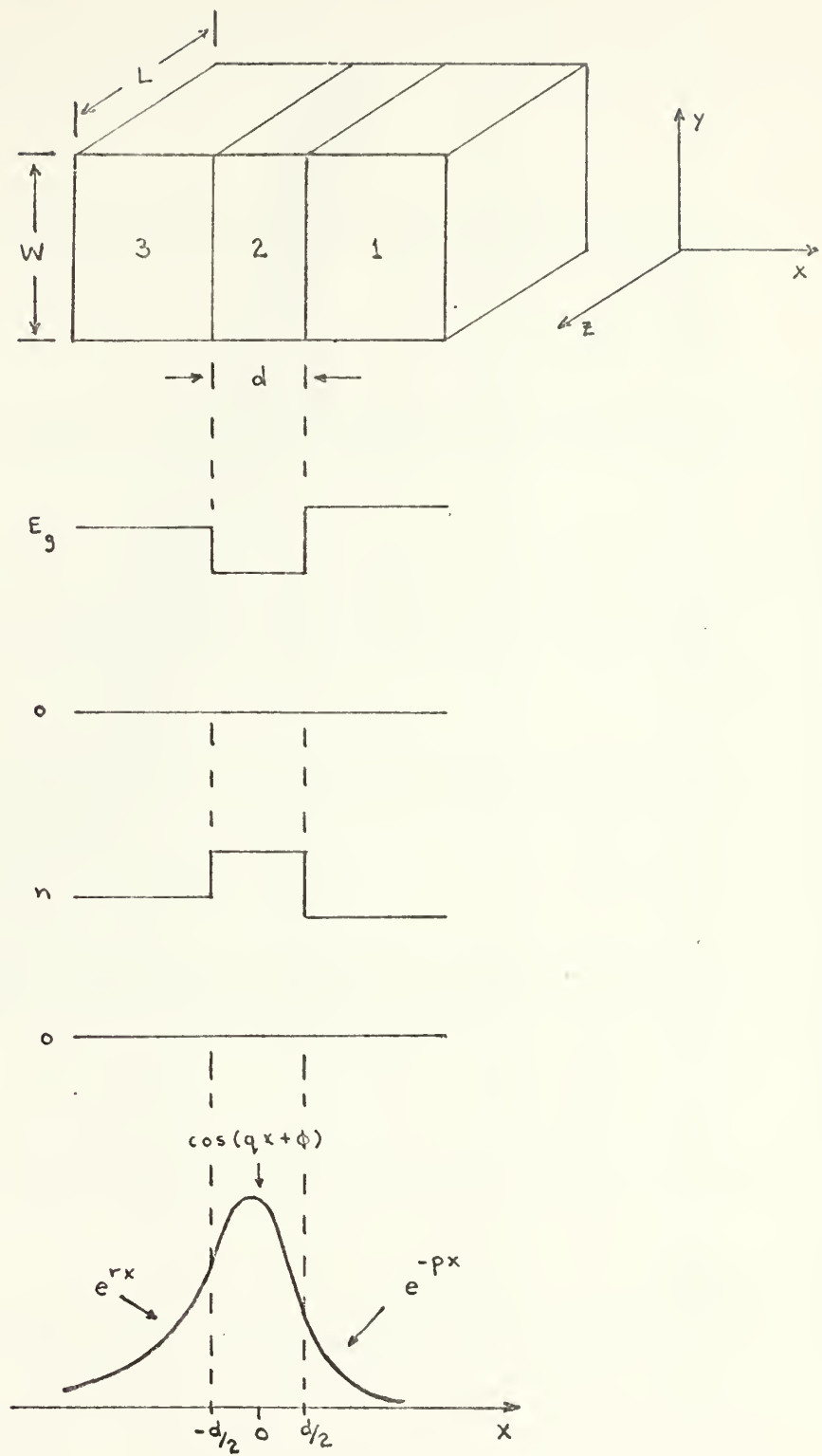


FIGURE 2-3. Three layer dielectric waveguide model



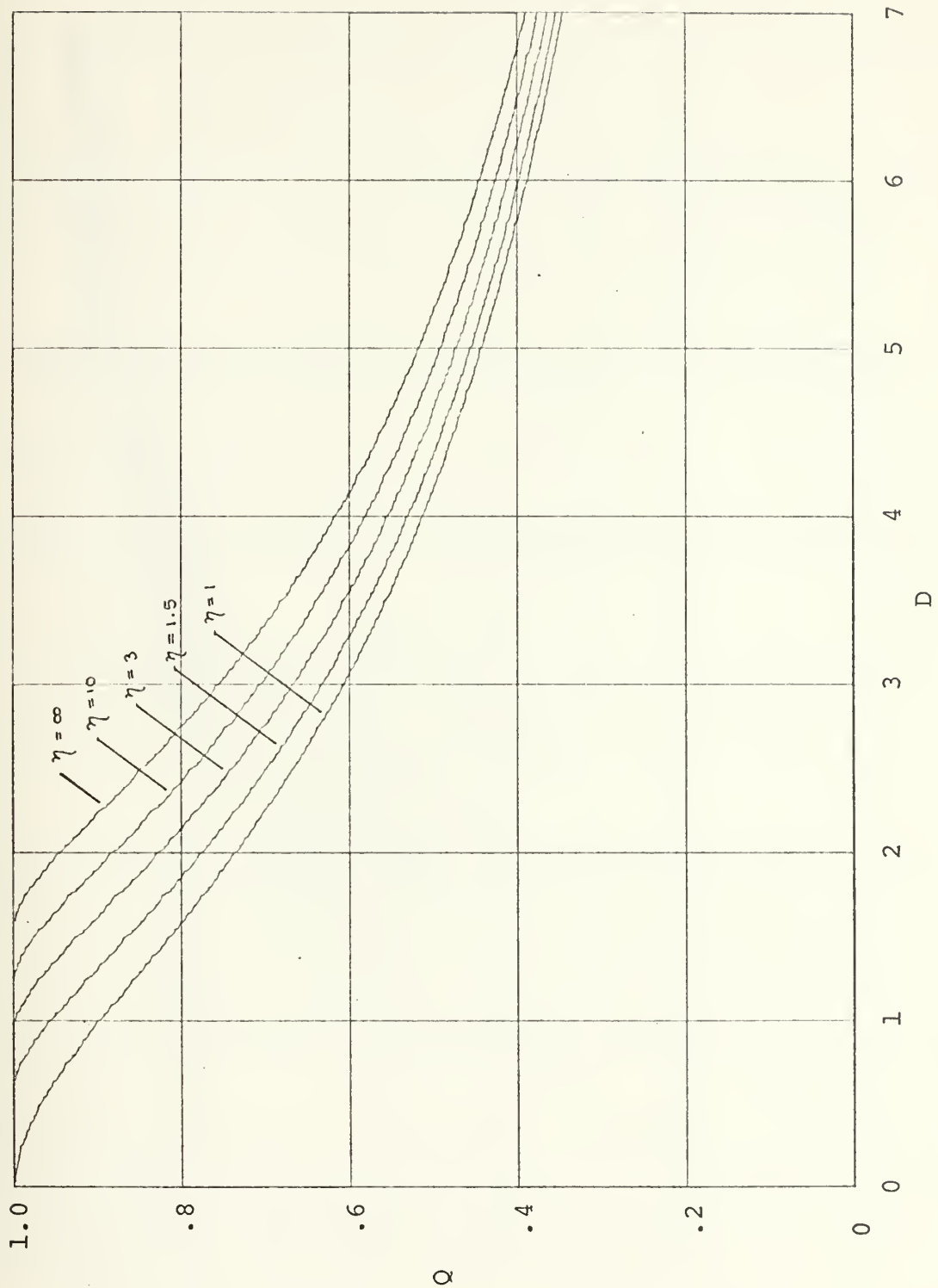


FIGURE 2-3. Normalized transverse propagation constant for region 2



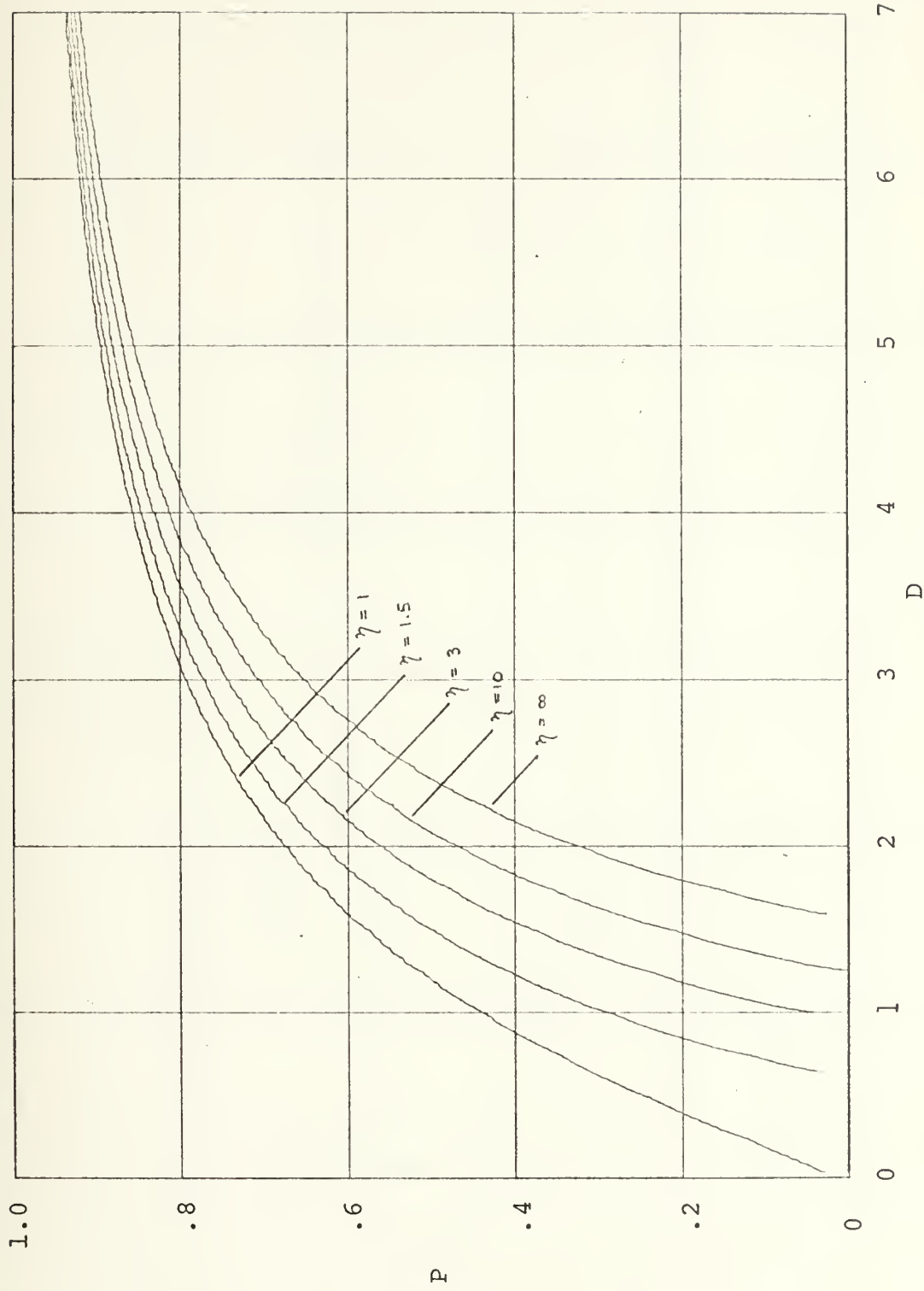


FIGURE 2-4. Normalized transverse propagation constant for region 1



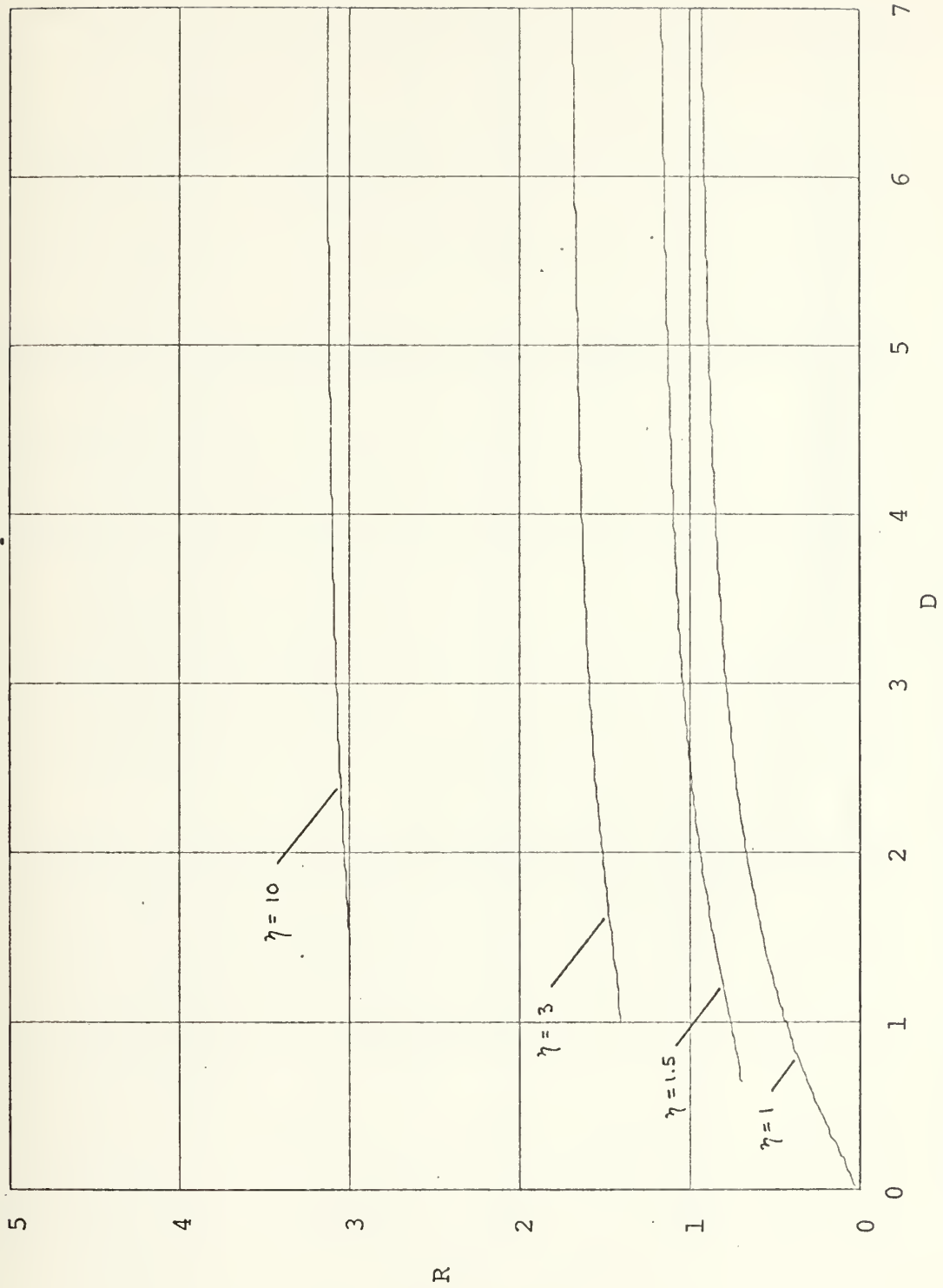


FIGURE 2-5. Normalized transverse propagation constant for region 3



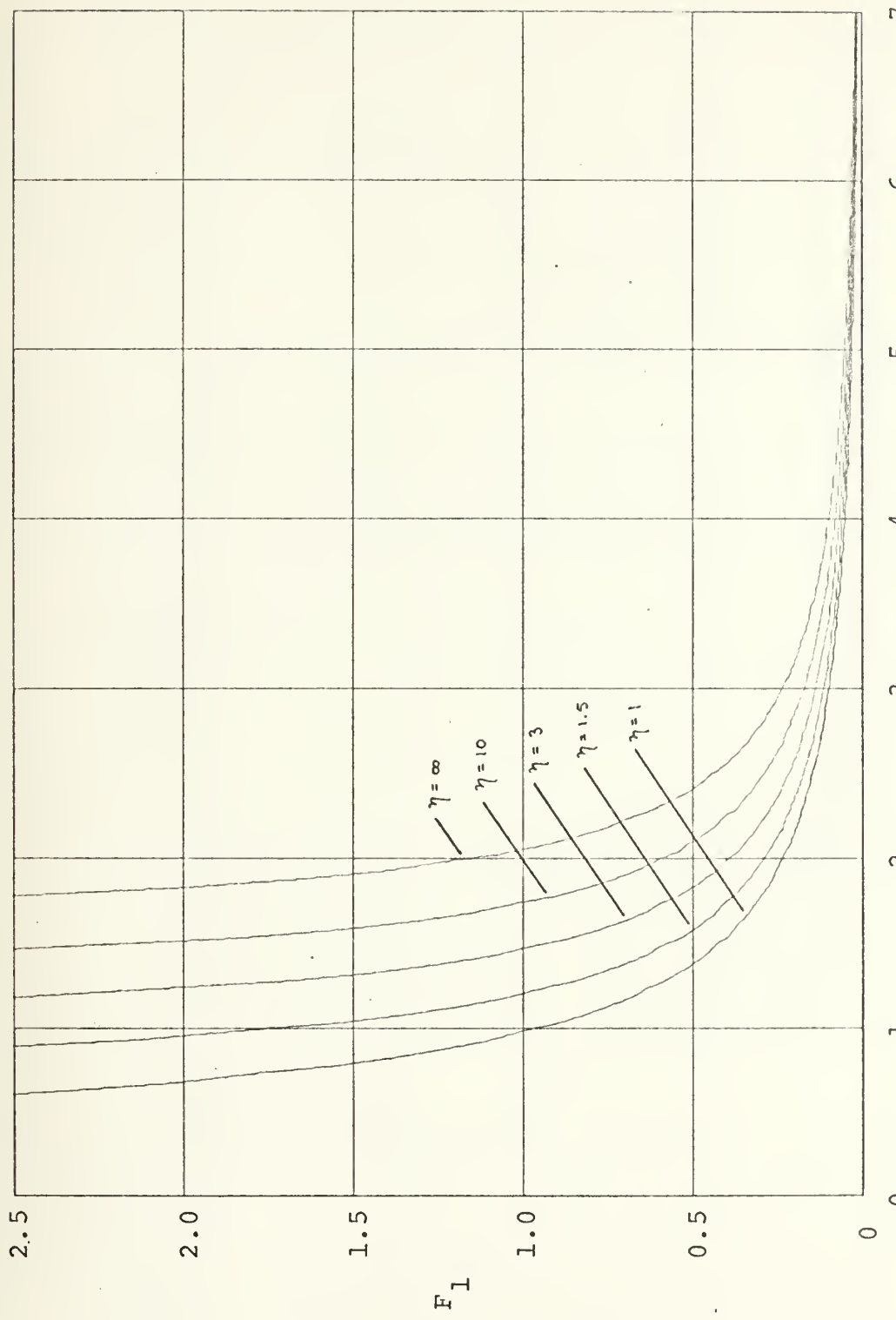


FIGURE 2-6. Loss factor for region 1



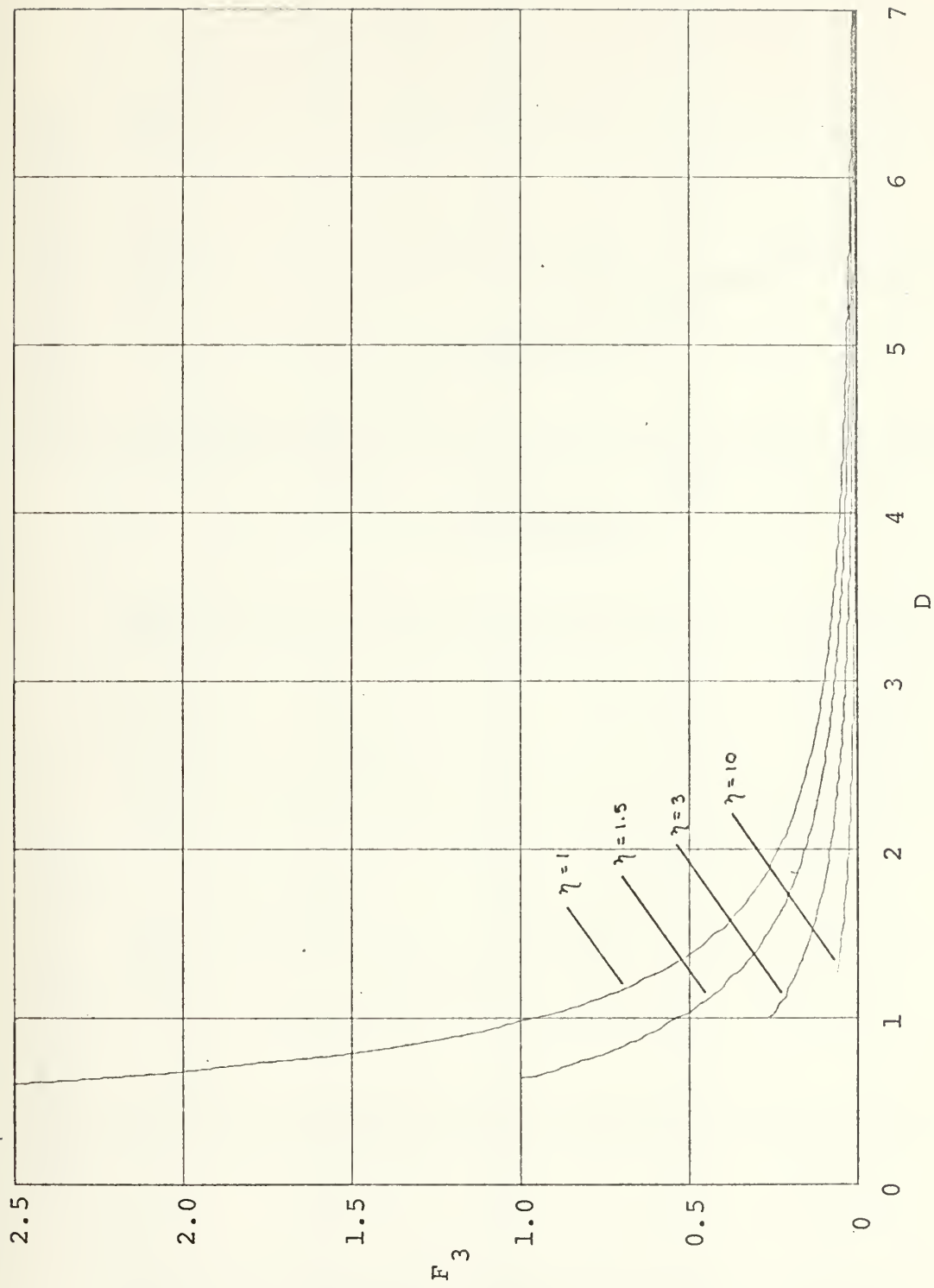


FIGURE 2-7. Loss factor for region 3



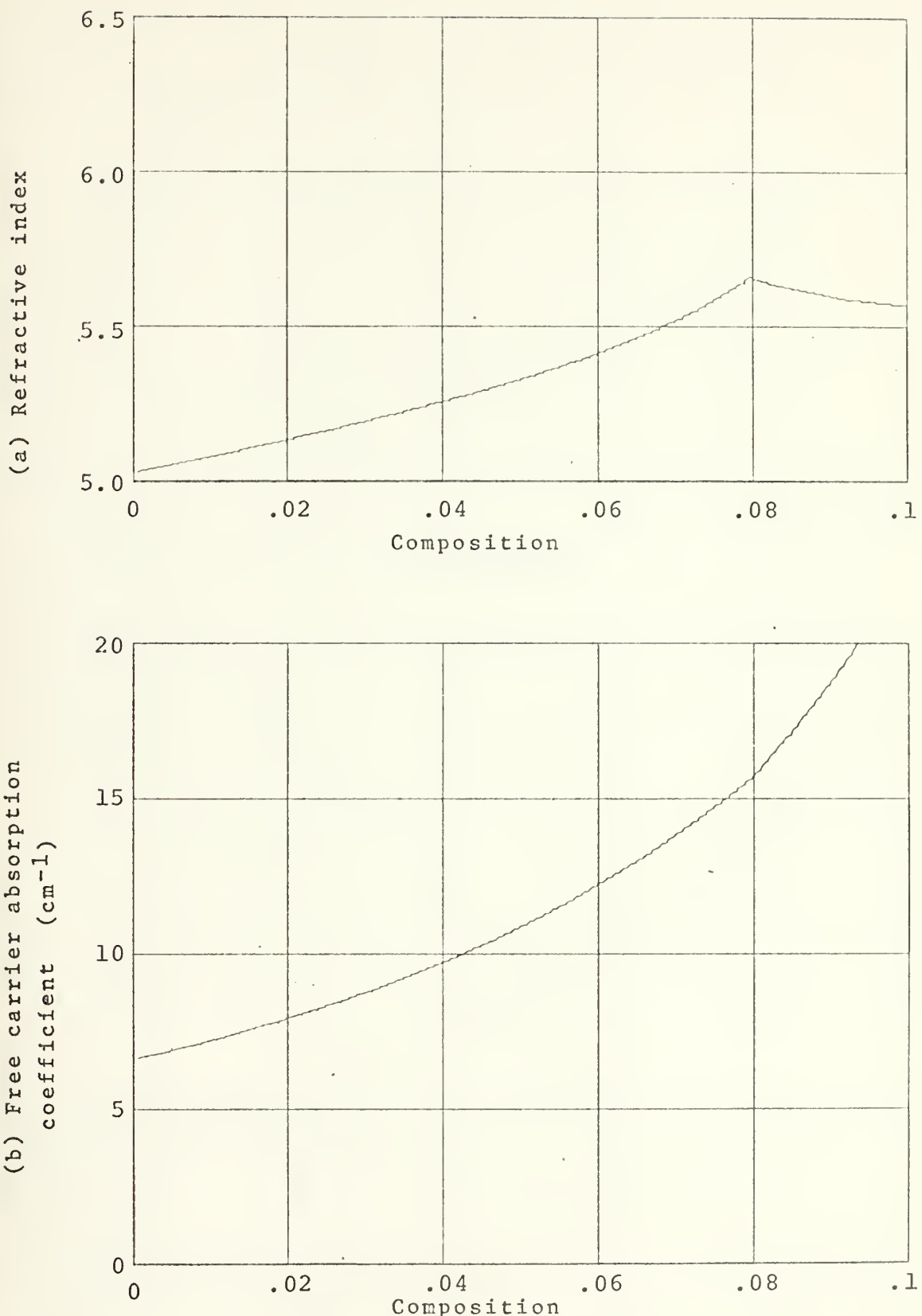


FIGURE 2-8. Refractive index and absorption coefficient of  $\text{Pb}_{1-y}\text{SnySe}$  at  $10.6\mu$



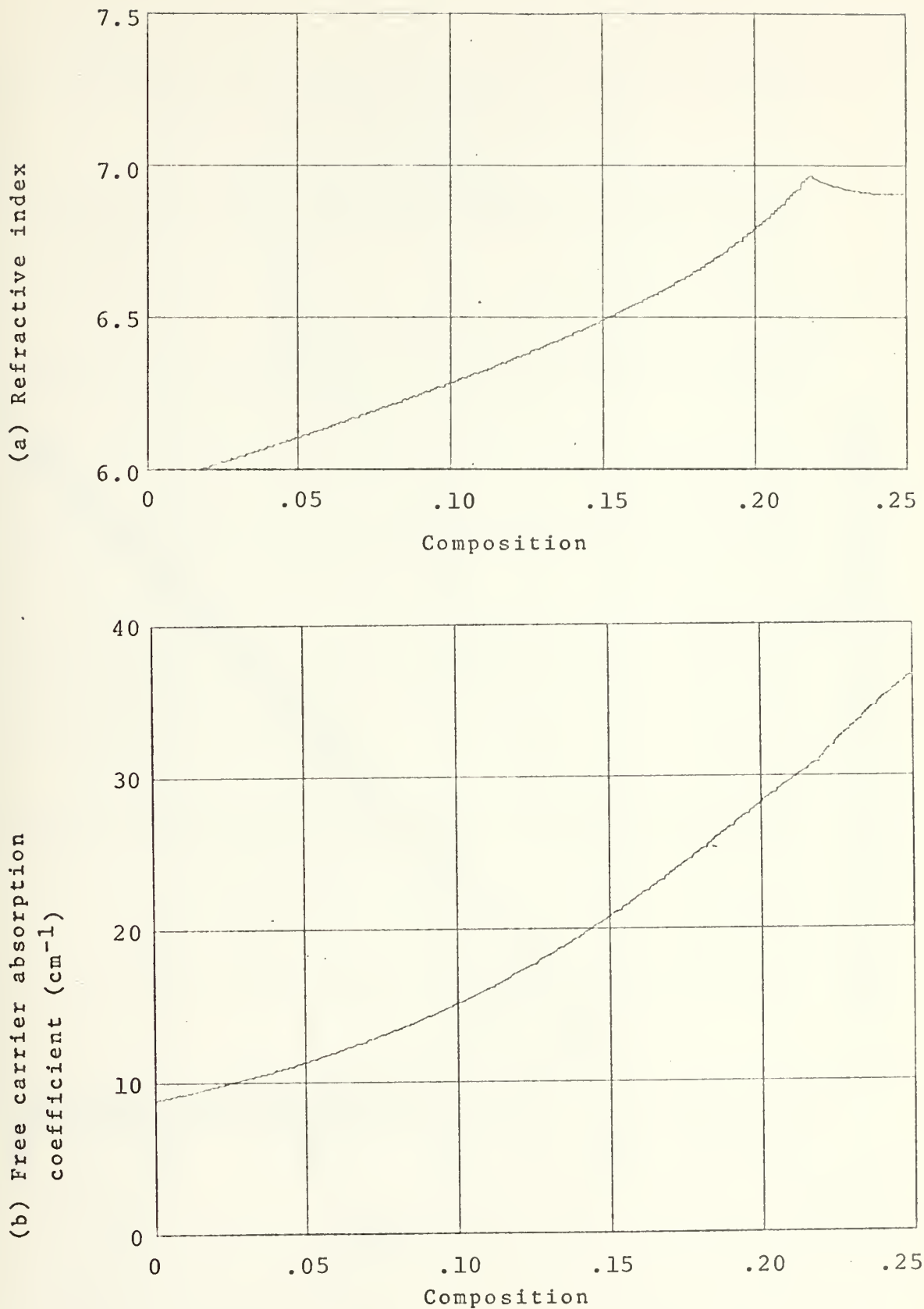


FIGURE 2-9. Refractive index and absorption coefficient of  $\text{Pb}_{1-x}\text{Sn}_x\text{Te}$  at  $10.6\mu$



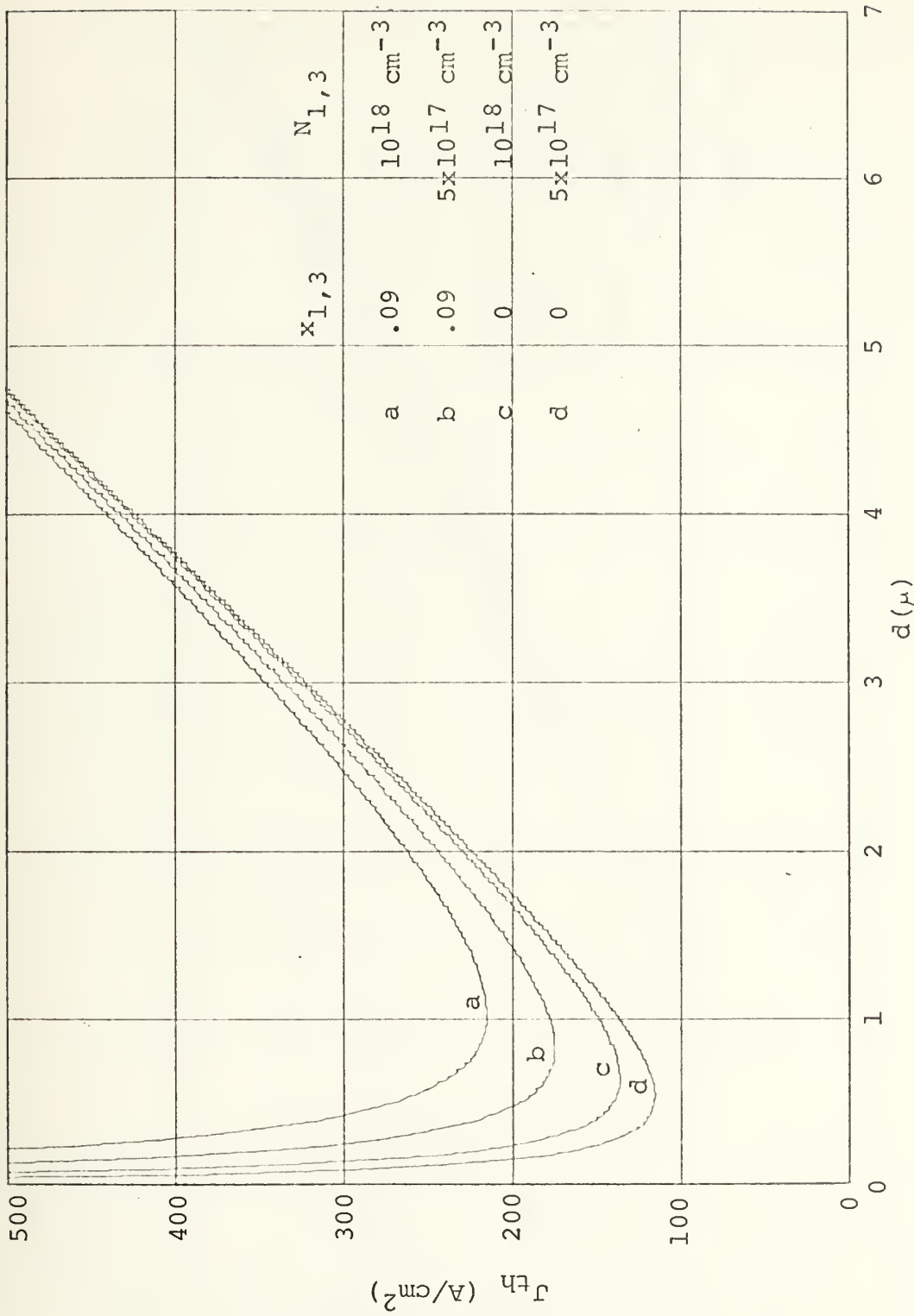


FIGURE 2-10. Threshold current density as a function of active region thickness for DH  $\text{Pb}_{1-x}\text{Sn}_x\text{Te}$  lasers



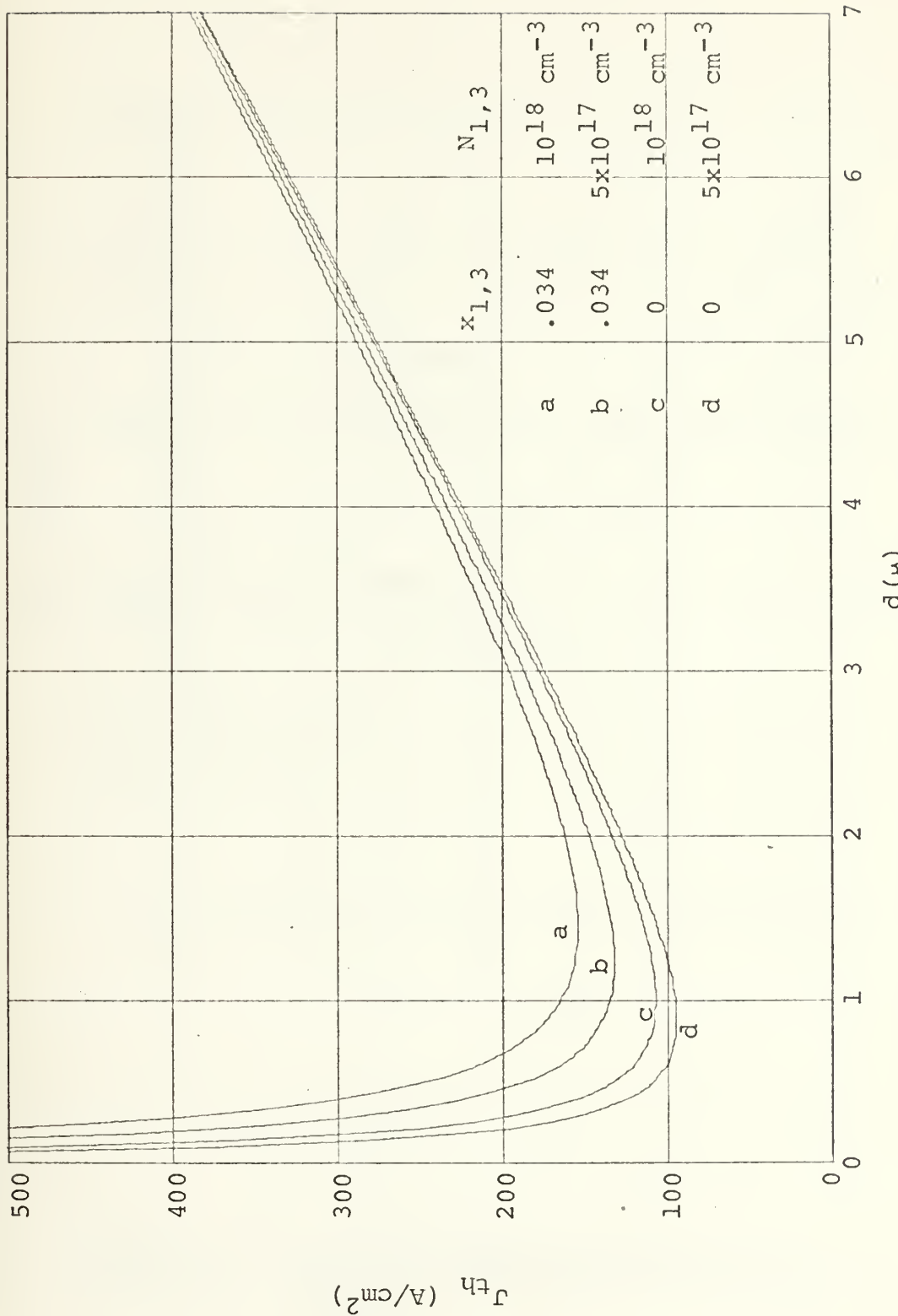


FIGURE 2-11. Threshold current density as a function of active region thickness for DH  $\text{Pb}_{1-y}\text{Sn}_y\text{Se}$  lasers



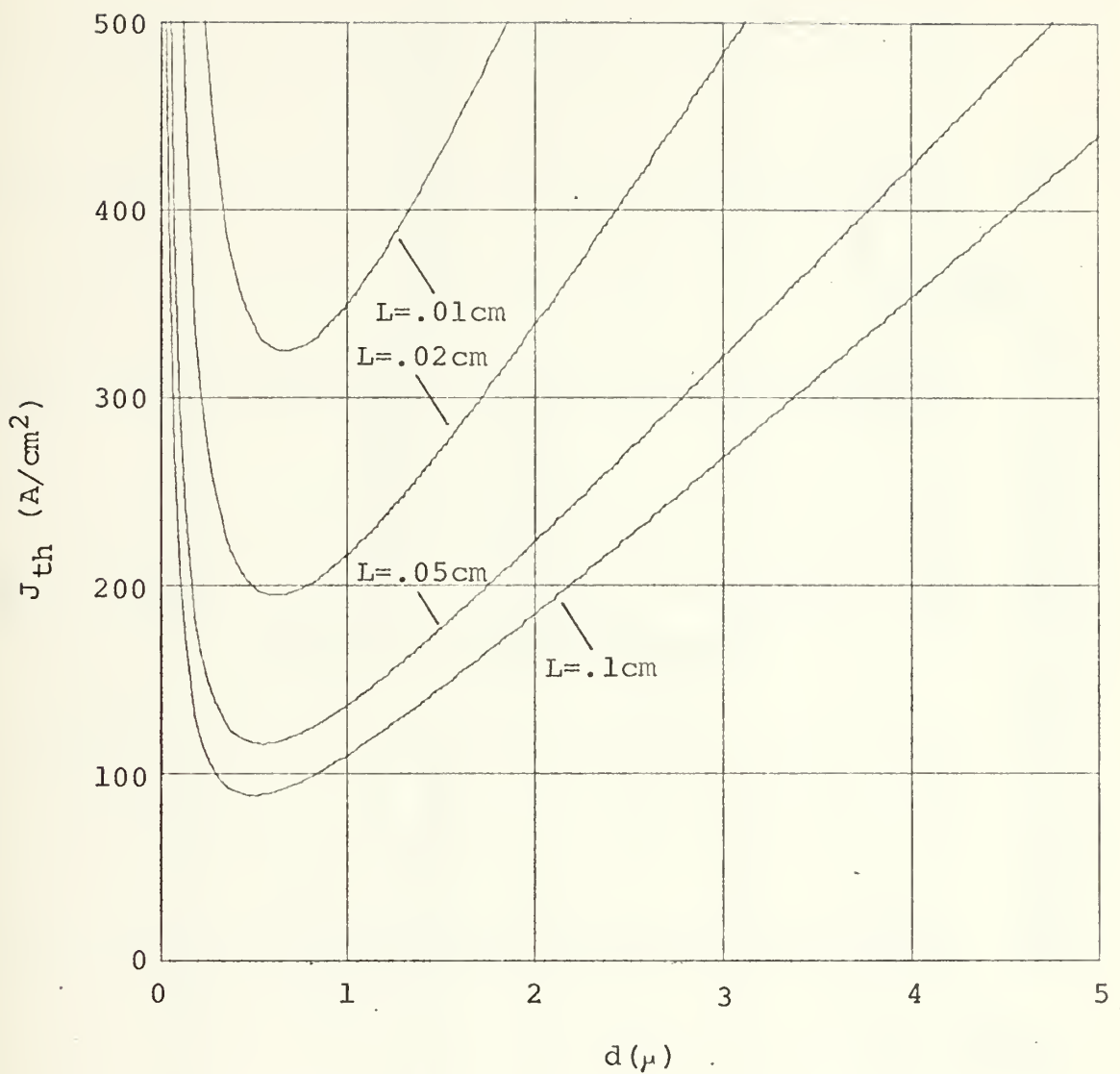


FIGURE 2-12. Threshold current density for  $\text{Pb}_{1-x}\text{Sn}_x\text{Te}$  DH lasers of various lengths



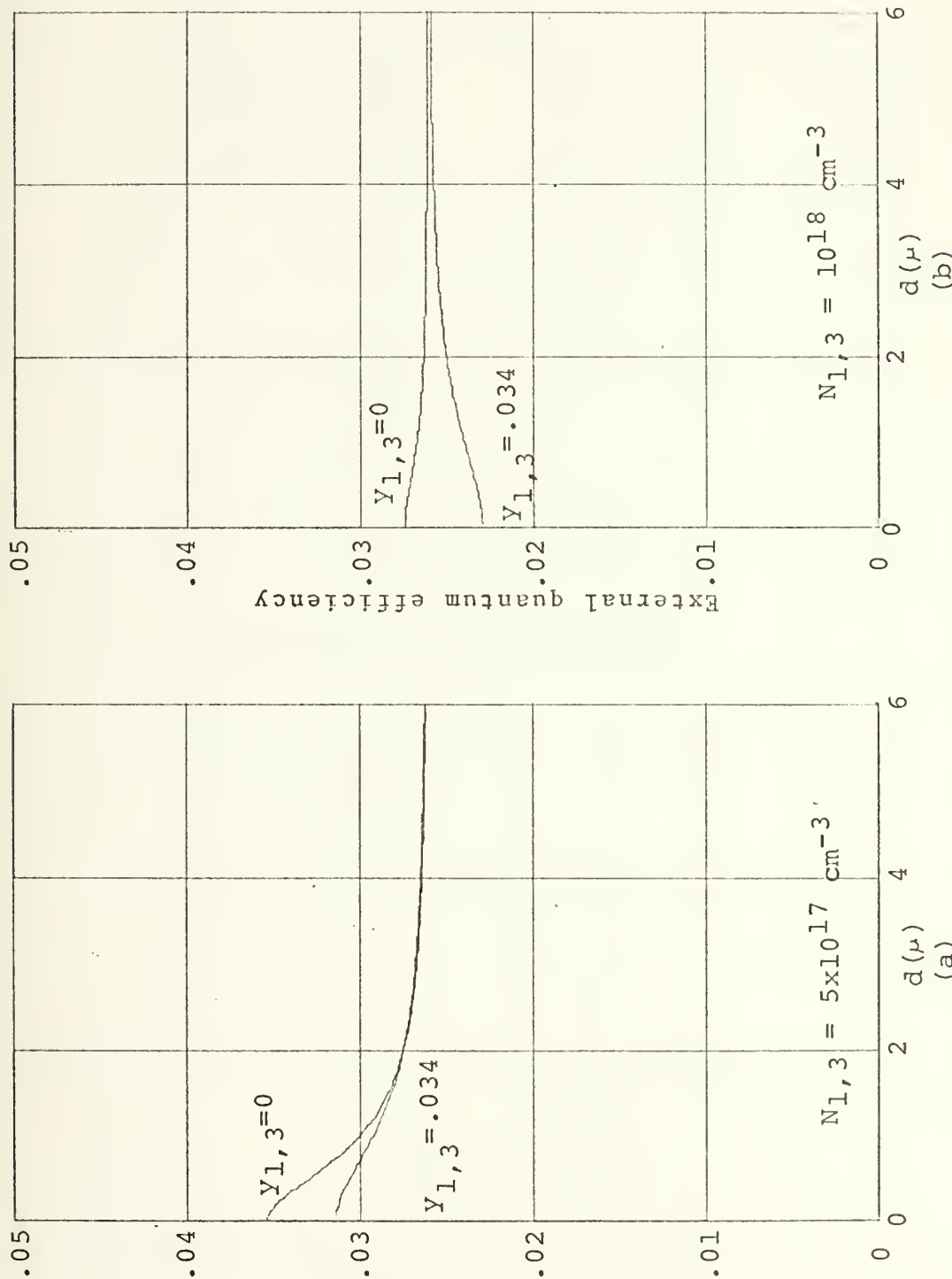
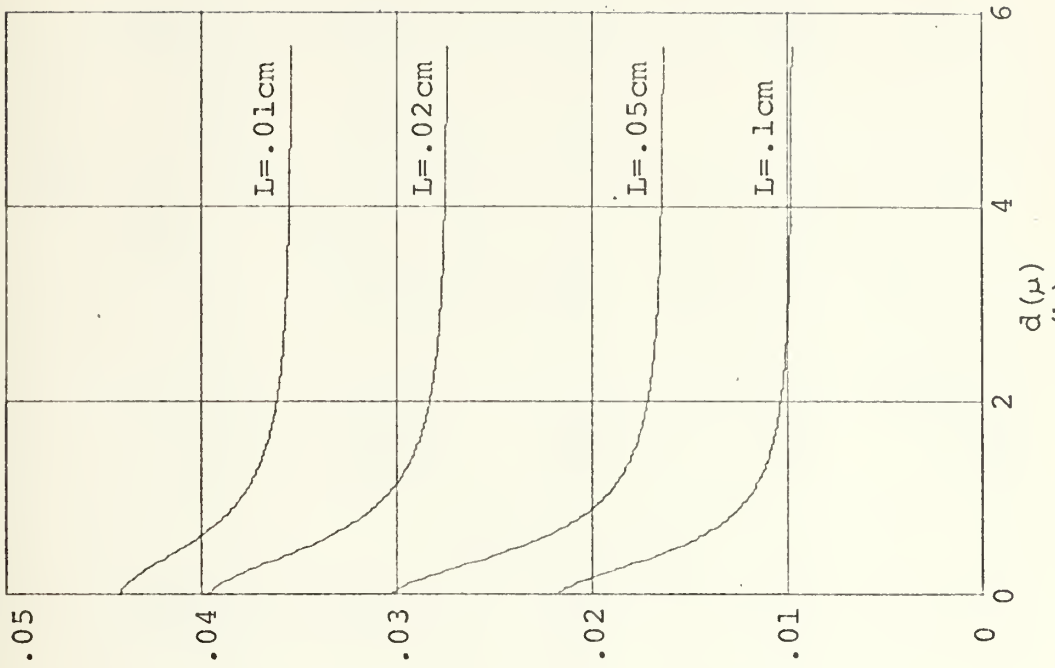


FIGURE 2-13. External quantum efficiency vs. active region thickness for  $\text{Pb}_{1-y}\text{SnySe}$  DH lasers





External quantum efficiency

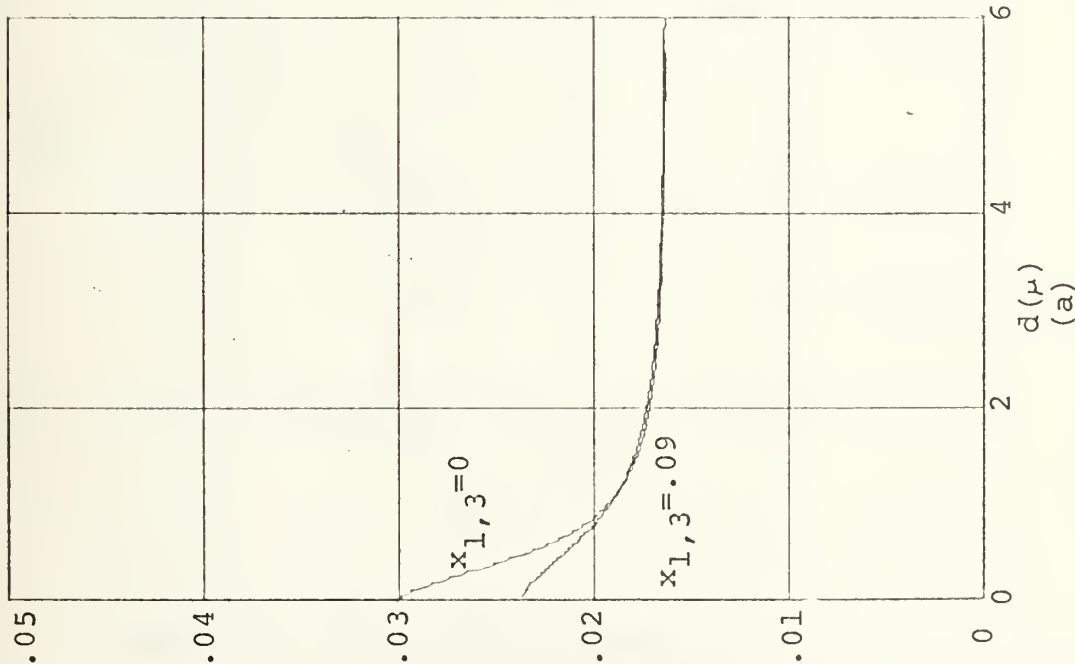
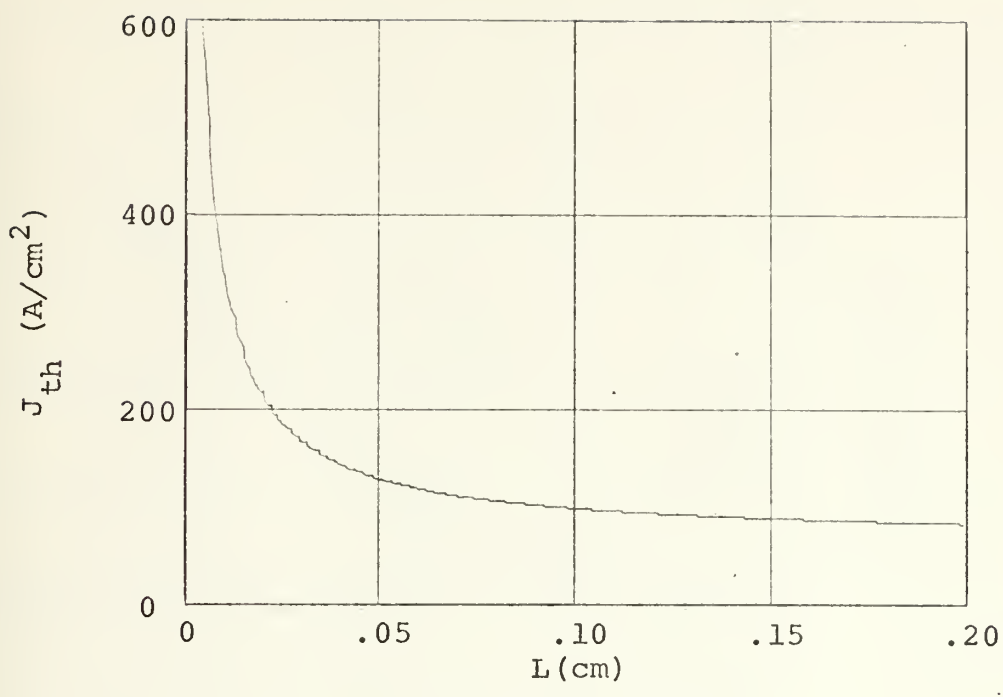


FIGURE 2-14. External quantum efficiency vs. active region thickness for  $\text{Pb}_{1-x}\text{Sn}_x\text{Te}$  DH lasers

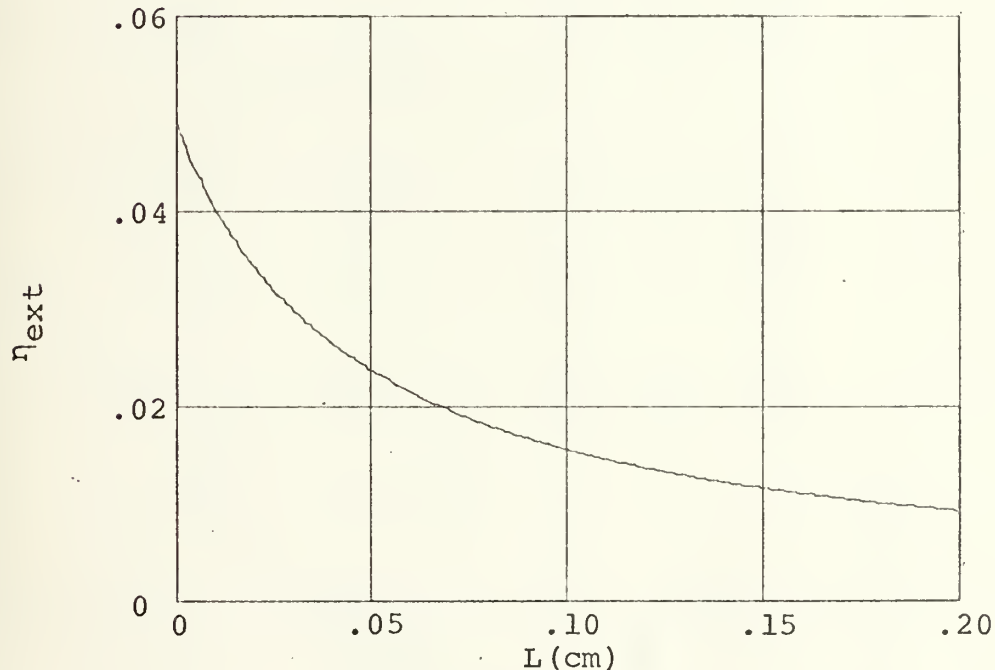
(a)

(b)





(a)  $J_{th}$  vs.  $L$



(b)  $\eta_{ext}$  vs.  $L$

FIGURE 2-16. Threshold current and external quantum efficiency as functions of cavity length for DH  $Pb_{1-x}Sn_xTe$  lasers,  $x_{1,3}=0$ ,  $N_{1,3} = 5 \times 10^{17} \text{ cm}^{-3}$



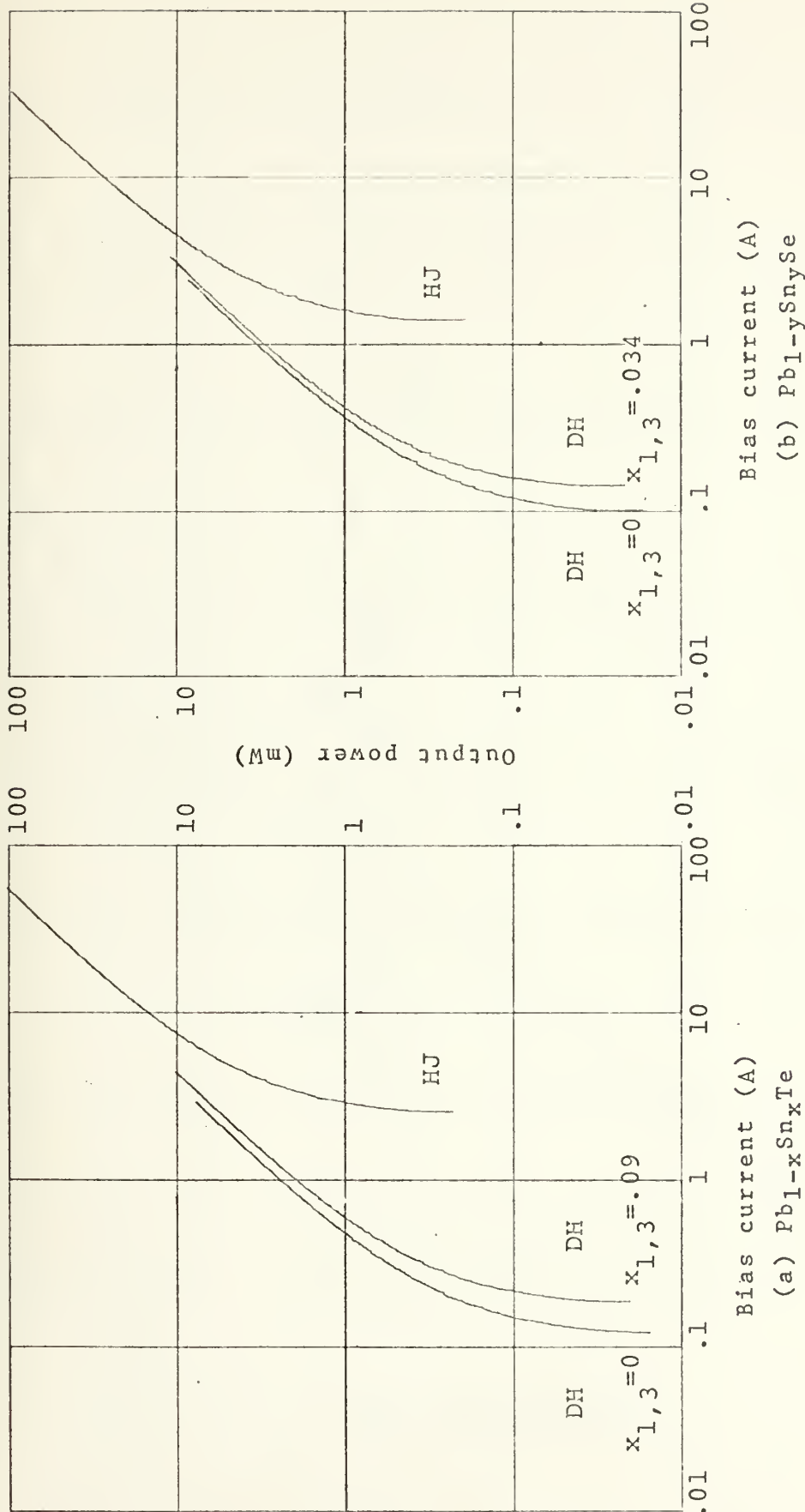


FIGURE 2-16. Output power as a function of bias current for  $Pb_{1-x}Sn_xTe$  and  $Pb_{1-y}SnySe$  injection lasers



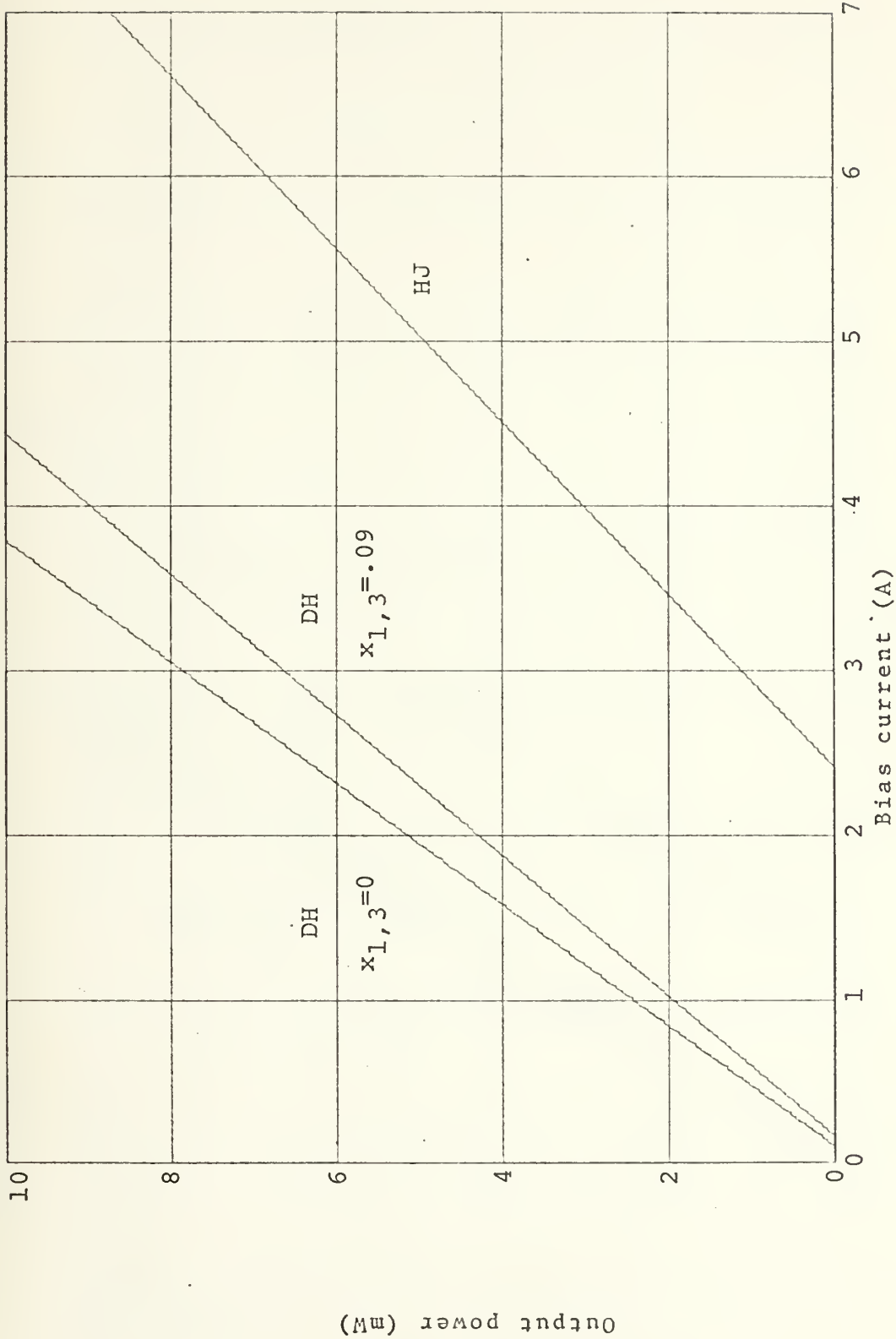


FIGURE 2-17. Output power vs. bias current for  $Pb_{1-x}Sn_xTe$  injection lasers



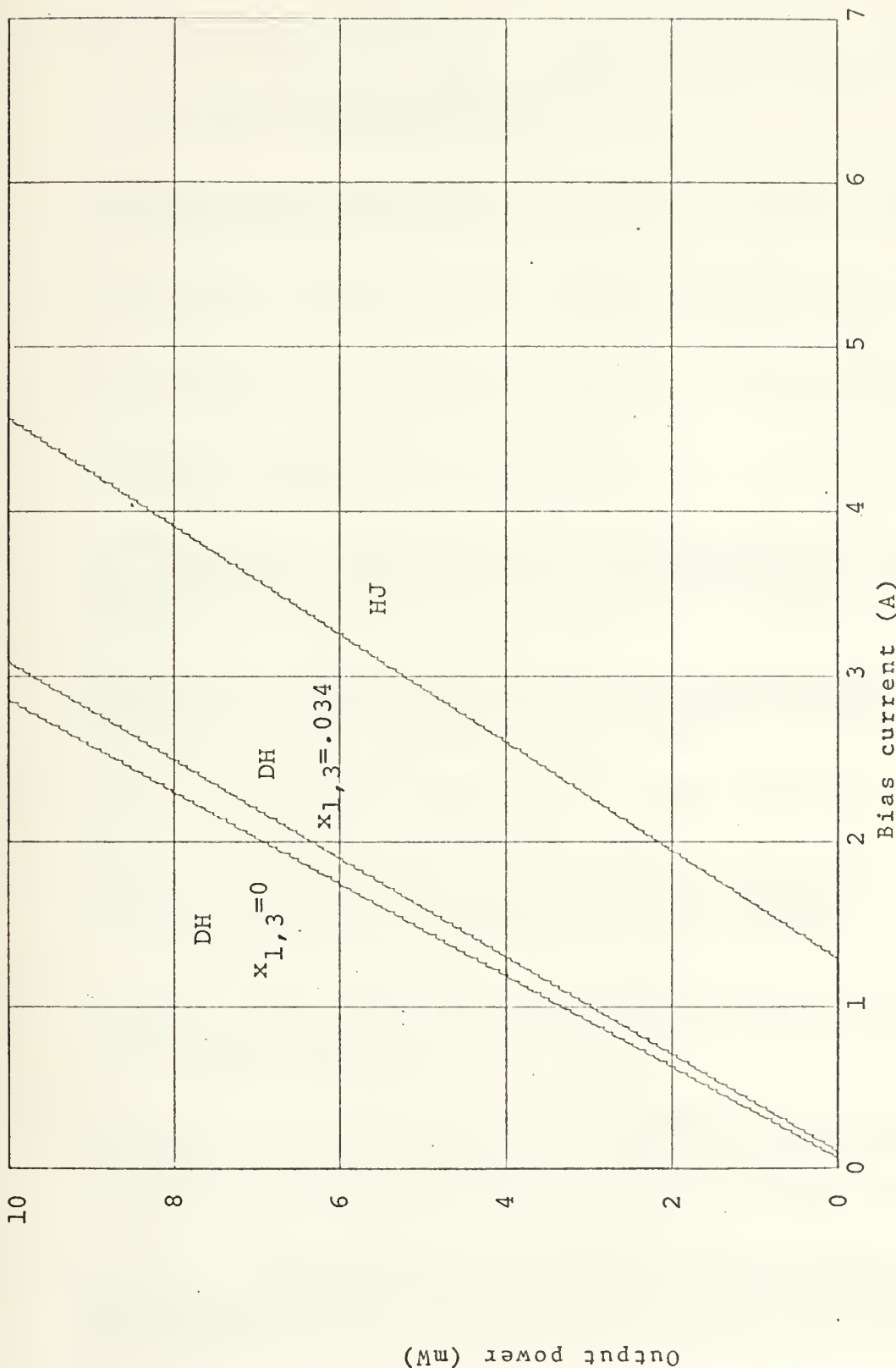


FIGURE 2-18. Output power vs. bias current for  $\text{Pb}_{1-y}\text{SnySe}$  injection lasers



### LIST OF REFERENCES

1. Mooradian, A., Strauss, A.J., and Rossi, J.A., "Broad-Band Laser Emission from Optically Pumped  $\text{PbS}_{1-x}\text{Se}_x$ ," IEEE Journal of Quantum Electronics, v. 9, no. 2, p. 347-249, 2 February 1973.
2. Harman, T.C., "Narrow-Gap Semiconductor Lasers," Journal of Physics and Chemistry of Solids, v. 32, sup. 1, p. 363-382, 1971.
3. Solid State Research Report, Lincoln Laboratory, M.I.T., p. 50-54, 1971:4.
4. Solid State Research Report, Lincoln Laboratory, M.I.T., p. 5-7, 1972:1.
5. Solid State Research Report, Lincoln Laboratory, M.I.T., p. 19-22, 1972:2.
6. Melngailis, I. and Harman, T.C., "Single-Crystal Lead-Tin Chalcogenides," Semiconductors and Semimetals, ed. Willardson and Beer, v. 5, p. 111-174, Academic Press, 1970.
7. Teich, M.C., "Coherent Detection in the Infrared," Semiconductors and Semimetals, ed. Willardson and Beer, v. 5, p. 361-407, Academic Press, 1970.
8. Moss, T.S., Optical Properties of Semi-conductors, p. 1-33, Academic Press, 1959.
9. Stern, F., "Dispersion of the Index of Refraction Near the Absorption Edge of Semiconductors," Physical Review, v. 133, no. 6A, p. A1653-A1664, 16 March 1964.
10. Riedl, H.R. and Scholar, R.B., "Dispersion of the Refractive Index Near the Fundamental Absorption Edge in  $\text{PbS}$ ," Physical Review, v. 131, no. 5, p. 2082-2083, 1 September 1963.
11. Strauss, A.J., and Harman, T.C., Pseudobinary Phase Diagram and Existence Regions for  $\text{PbS}_{1-x}\text{Se}$ , paper presented at Conference on the Physics of IV-VI Compounds and Alloys, Philadelphia, Pennsylvania, March 1972.
12. Kim, M.E., The Optical Properties and Energy Gap of Thin Lead Tin Selenide Films in the Fundamental Absorption Edge Region, M.S.E.E. Thesis, University of California, Los Angeles, 1971.



13. Walz, V.M., The Determination of Optical Properties and Energy Gap of  $Pb_{1-x}Sn_xTe$  Thin Films in the Fundamental Absorption Edge Region, M.S.E.E., Thesis, Naval Post-graduate School, Monterey, 1972.
14. Tao, T.F., Private Communication, Naval Postgraduate School, Monterey, California.
15. Tansley, T.L., "Heterojunction Properties," Semiconductors and Semimetals, ed. Willardson and Beer, v. 7, p. 293-368, Academic Press, 1971.
16. Kressel, H., "Semiconductor Lasers," Lasers, ed. Levine and DeMaria, v. 3, p. 1-110, Marcel Dekker, 1971.
17. Sze, S.M., Physics of Semiconductor Devices, Wiley, 1969.
18. Sahai, R., and Milnes, A.G., "Heterojunction Solar Cell Calculations," Solid-State Electronics, v. 13, p. 1289-1299, Pergamon Press, 1970.
19. Hovel, H.J., Woodall, J.M., and Howard, W.E., The Spectral Response and Conversion Efficiency of  $Gal-xAl_xAs$ -GaAs Solar Cells, paper presented at Symposium on GaAs, Boulder, Colorado, September 1972.
20. Fernandez, J.M., Study of Heterojunction  $Pb_{1-x}Sn_xTe$  Diodes, M.S.E.E., Thesis, Naval Postgraduate School, Monterey, California, 1972.
21. Panish, M.B., and Hayashi, I., "A New Class of Diode Lasers," Scientific American, p. 32-40, July 1971.
22. Adams, M.J., and Landsberg, P.T., "The Theory of the Injection Laser," Gallium Arsenide Lasers, ed. Gooch, p. 5-79, Wiley, 1969.
23. Anderson, W.W., "Mode Confinement and Gain in Junction Lasers," IEEE Journal of Quantum Electronics, v. QE-1, no. 6, p. 228-236, September 1965.
24. Holloway, H. and others, "Injection Luminescence and Laser Action in Epitaxial PbTe Diodes," Applied Physics Letters, v. 21, no. 1, p. 5-6, 1 July 1972.
25. Donnelly, J.P. and others, "Pb<sub>1-x</sub>Sn<sub>x</sub>Te Photovoltaic Diodes and Diode Lasers Produced by Proton Bombardment," Solid-State Electronics, v. 15, p. 403-407, Pergamon Press, 1972.



26. Tao, T.F. and Wang, C.C., "Narrow Gap Semiconductors  $Pb_{1-x}Sn_xTe$  and  $Pb_{1-y}Sn_ySe$ ," Air Force Materials Laboratory Technical Report TR-71-238, December 1971.
27. Ralstion, R.W., and others, "Stripe-Geometry  $Pb_{1-x}Sn_xTe$  Diode Lasers," IEEE Journal of Quantum Electronics, v. QE-9, no. 2, p. 350-356, February 1973.
28. Logothetis, E.M. and others, "Infrared Detection by Schottky Barriers in Epitaxial PbTe," Applied Physics Letters, v. 19, no. 9, p. 318-320, 1 November 1971.
29. Solid State Research Report, Lincoln Laboratory, M.I.T., p. 1-4, 1973:1.
30. Antcliffe, G.A. and Wrobel, J.S., "Spontaneous and Laser Emission From  $Pb_{1-x}Sn_xTe$  Diodes Prepared by Sb Diffusion," Applied Physics Letters, v. 17, no. 7, p. 290-292, October 1970.
31. Butler, J.F. and Harman, T.C., "Long-Wavelength Infrared  $Pb_{1-x}Sn_xTe$  Diode Lasers," Applied Physics Letters, v. 12, no. 10, p. 347-349, 15 May 1968.
32. Norton, P. and others, "Extended Wavelength Tuning of Pb Sn Te Lasers," Applied Physics Letters, v. 18, no. 4, p. 158-159, 15 February 1971.



INITIAL DISTRIBUTION LIST

No. Copies

1. Defense Documentation Center Cameron Station Alexandria, Virginia 22314	2
2. Library, Code 0212 Naval Postgraduate School Monterey, California 93940	2
3. Assc. Professor Tien F. Tao, Code 52 Tv Department of Electrical Engineering Naval Postgraduate School Monterey, California 93940	5
4. ENS Walter G. Opyd USN 118 Wilson Ave. Vallejo, California 94590	2



## DOCUMENT CONTROL DATA - R &amp; D

(Security classification of title, body of abstract and indexing annotation must be entered when the overall report is classified)

ORIGINATING ACTIVITY (Corporate author)	2a. REPORT SECURITY CLASSIFICATION
	Unclassified

Naval Postgraduate School  
Monterey, California 93940

2b. GROUP

REPORT TITLE  
The Refractive Index of  $Pb_{1-x}Sn_xTe$ ,  $Pb_{1-y}Sn_ySe$ , and  $PbS_{1-x}Se_x$   
and Theoretical Calculations for  $Pb_{1-x}Sn_xTe$  and  $Pb_{1-y}Sn_ySe$  10.6 $\mu$   
Micron Heterostructure Injection lasers.

DESCRIPTIVE NOTES (Type of report and, inclusive dates)  
Master's Thesis; (June 1973)

AUTHOR(S) (First name, middle initial, last name)

Walter George Opyd

REPORT DATE June 1973	7a. TOTAL NO. OF PAGES	7b. NO. OF REFS
CONTRACT OR GRANT NO.	9a. ORIGINATOR'S REPORT NUMBER(S)	
PROJECT NO.	9b. OTHER REPORT NO(S) (Any other numbers that may be assigned this report)	

DISTRIBUTION STATEMENT

Approved for public release; distribution unlimited.

SUPPLEMENTARY NOTES	12. SPONSORING MILITARY ACTIVITY Naval Postgraduate School Monterey, California 9 940
---------------------	---

ABSTRACT

In the first part of this work, the refractive indices,  $n$ , in the fundamental absorption edge regions of three alloy semiconductors,  $Pb_{1-x}Sn_xTe$ ,  $Pb_{1-y}Sn_ySe$ , and  $PbS_{1-x}Se_x$ , were investigated. Preliminary results of the refractive indices of  $PbS_{1-x}Se_x$  thin films are presented. For  $Pb_{1-x}Sn_xTe$  and  $Pb_{1-y}Sn_ySe$ , empirical relationships for  $n$  have been determined as a function of wavelength, composition, and temperature, using refractive index data previously measured in this laboratory. In the second part of this work, the laser performances of double heterojunction  $Pb_{1-x}Sn_xTe$  and  $Pb_{1-y}Sn_ySe$  injection lasers emitting 10.6 $\mu$  radiation and operated at 85°K, were theoretically calculated. Threshold current and lasing output power as functions of compositions and laser geometry, were calculated as a guide for optimum design. Threshold current densities of less than 200A/cm<sup>2</sup> and output power of more than 2mW with 1A bias current were calculated for diodes of 1mm<sup>2</sup> cross section, operated at 85°K.



KEY WORDS	LINK A		LINK B		LINK C	
	ROLE	WT	ROLE	WT	ROLE	WT
Pb <sub>1-x</sub> Sn <sub>x</sub> Te						
Pb <sub>1-y</sub> Sn <sub>y</sub> Se						
Refractive Index						
Laser						
Heterojunction						



Thesis

145476

05834 Opyd

c.1

The refractive index  
of  $Pb_{1-x}^x Sn Te$ ,  $Pb_{1-y}^y$   
 $Sn Se$ , and  $PbS_{1-x}^x Se_y^y$  and  
theoretical calculations  
for  $Pb_{1-x}^x Sn Te$  and  $Pb_{1-y}^y$   
 $Sn Se$  10.6 micron hetero-  
structure injection  
lasers.

Thesis

145476

05834 Opyd

c.1

The refractive index  
of  $Pb_{1-x}^x Sn Te$ ,  $Pb_{1-y}^y$   
 $Sn Se$ , and  $PbS_{1-x}^x Se_y^y$  and  
theoretical calculations  
for  $Pb_{1-x}^x Sn Te$  and  $Pb_{1-y}^y$   
 $Sn Se$  10.6 micron hetero-  
structure injection  
lasers.

thes05834  
The refractive index of Pb(1-x)Sn(x)Te,



3 2768 001 00067 2  
DUDLEY KNOX LIBRARY